Toward Automated Ice-Water Classification on Large Northern Lakes Using RADARSAT-2 Synthetic Aperture Radar Imagery

by

Marie Hoekstra

A thesis
presented to the University of Waterloo
in fulfillment of the
thesis requirement for the degree of
Master of Science
in
Geography

Waterlo, Ontario, Canada, 2018

Authors Declaration

I hereby declare that I am the sole author of this thesis. This is a true copy of the thesis, including any required final revisions, as accepted by my examiners. I understand that my thesis may be made electronically available to the public.

Abstract

Changes to ice cover on lakes throughout the northern landscape has been established as an indicator of climate change and variability. These changes are expected to have implications for both human and environmental systems. Additionally, monitoring lake ice cover is required to enable more reliable weather forecasting across lake-rich northern latitudes. Currently the Canadian Ice Service (CIS) monitors lakes using RADARSAT-2 SAR (synthetic aperture radar) and optical imagery through visual interpretation, with total lake ice cover reported weekly as a fraction out of ten. An automated method of classification would allow for more detailed records to be delivered operationally.

In this research, the Iterative Region Growing using Semantics (IRGS) approach has been employed to perform ice-water classification on 61 RADARSAT-2 scenes of Great Bear Lake and Great Slave Lake over a three year period. This approach first locally segments homogeneous regions in an image, then merges similar regions into classes across the entire scene. These classes are manually labelled by the user, however automated labelling capability is currently in development. An accuracy assessment has been performed on the classification results, comparing outcomes with user-generated reference data as well as the CIS fraction reported at the time of image acquisition. The overall average accuracy of the IRGS method for this dataset is 92%, demonstrating the potential of this semi-automated method to provide detailed and reliable lake ice cover information.

Acknowledgements

I would first like to extend my sincere gratitude to my thesis advisor Professor Claude Duguay for the opportunity to do this research, and for his continuous encouragement, advice, and especially patience. I would also like to thank him for the learning and life experience I was able gain through conference and workshop attendance as his student. He always made himself available to provide guidance and feedback throughout the creation of this work and I am very thankful for it.

I would also like to thank my co-advisor Professor David Clausi for providing guidance to shape the direction of this work, and for educating me on the technical aspects of remote sensing and on matters of image processing. Our weekly meetings helped to make sense of topics which seemed incomprehensible to me upon first glance. My appreciation also extends to Linlin Xu, Ross Duquette, Michael Stone, and Mingzhe Jiang from the Vision and Imaging Processing lab for their work on MAGIC and for answering my endless questions. I would also like to express my appreciation to Véronique Pinard from the Canadian Ice Service for helping with validation and answering my many questions.

I would like to acknowledge Stephen Howell and Professor Andrea Scott for their participation on my thesis committee. Many thanks to Junqian Wang for her discussions, comradery, and encouragement, and to Kevin Kang for his guidance.

Lastly, I would like to thank my dear, wonderful family as well as Clara Greig, Nick Wilson, Evan Wilcox, Sarah Godding, Caitlin Price, and Matt Gilmour for their endless reassurance, encouragement, and sense of humor. This work would not have been possible without the inspiration and support I received from all of these yahoos.

Table of Contents

List of Figures

List of Tables

1.0 General Introduction

1.1 Introduction and Motivation

Lakes encompass a large part of the hydrological system of fresh water flowing throughout the Northern Hemisphere. In arctic and sub-arctic regions the areal extent of lakes cover 15-40% of the landscape (Duguay et al., 2003). Seasonal ice on these lakes represents a significant component of the cryosphere and plays a role in many biologic, ecologic and socio-economic processes (Prowse et al., 2011b). A movement towards later freeze-up and earlier break-up dates on northern lakes since the middle of the last century has been demonstrated in various studies and is predicted to continue (Brown & Duguay, 2011; Duguay et al., 2006; Magnuson, 2000; Palecki & Barry, 1986). Alterations to the state of lake ice cover due to climate change is expected to have implications for both human and environmental systems. For example, transportation via ice roads has already begun to be affected by unusually mild winters. Continued climate warming will cause further challenges for those who rely on seasonal lake ice for access to isolated communities and remote industries (Prowse et al., 2011a). In addition, an increase in the duration of the open-water season will raise evaporation rates and impact lake-climate interactions.

The inclusion of lakes and lake ice in weather forecasting and climate models has also been advocated in recent literature. Some climate simulations do not account for the multitude of small lakes across Canada, however the simulations that do have presented more accurate results when compared with real-world observations (Brown & Duguay, 2010). Understanding, recording, and predicting lake ice phenology will be necessary for both local weather forecasting and overall climate modelling going forward (Brown & Duguay, 2010).

Ground observations of lake ice conditions have been gathered at a network of sites across the country since 1822. Unfortunately, since the 1980s the number of in-situ lake ice observations has plummeted as a result of budget cuts to government agencies as well as the advancement of remote sensing systems (Duguay et al., 2006; Lenormand et al., 2002). The launch of earth observing satellite systems has been able to increase the coverage and frequency of lake ice observations allowing for the creation of detailed lake ice phenology records, though this has yet to be realized (Jeffries et al., 2005). The literature on monitoring lake ice is not a large collection when compared to that of other aspects of the cryosphere despite the proven importance of lake ice phenology in the context of climate change (Jeffries et al., 2012).

Currently, the Canadian Ice Service (CIS) monitors ice cover on over 130 lakes across Canada using a combination of synthetic aperture radar (SAR) and optical imagery for use in numerical weather prediction models (Brown et al, 2002). SAR systems are particularly well suited for this application as they are unaffected by cloud cover and can acquire images overnight and during polar darkness. These scenes are visually interpreted, and ice cover is reported as a fraction out of ten on a weekly basis (Geldsetzer & van der Sanden, 2013; Howell et al., 2009). More detailed information including percent coverage, position, and extent of the lake ice is not available operationally as it would be time consuming and thus costly if produced in the existing manner. If an unsupervised method of classification were made operational, detailed records of ice extent on these lakes could be provided at high spatial and temporal resolutions. The need for such a method will soon become essential considering the wealth of operational SAR data that is becoming available from new satellite missions such as Sentinel 1 A/B and the upcoming RADARSAT Constellation Mission (RCM). Automated classification approaches using SAR imagery provide

a potential solution to fill the gap in lake ice research by allowing for precise, timely, and thus cost effective monitoring. This unmet potential underpins the motivation for this work.

1.2 Research Objective

The Vision and Image Processing (VIP) Lab at the University of Waterloo has developed a software system called MAGIC (MAp Guided Ice Classification). This system showcases the iterative region growing using semantics (IRGS) approach, which allows for semi-automated classification of SAR images. The IRGS approach has been proven a reliable method multiple times on SAR datasets of sea ice (Yu & Clausi, 2007; 2008; Leigh et al., 2014) but has not yet been applied to lake ice imagery. Because of its specialized nature, IRGS shows promise as a means to quickly and accurately provide high quality lake ice cover information. The MAGIC user interface (UI) also includes other segmentation methods to allow for comparison with IRGS (Clausi et al., 2010).

This study employs the IRGS method to classify ice and water in 61 RADARSAT-2 SAR scenes of large northern lakes, namely Great Bear Lake (GBL) and Great Slave Lake (GSL) located in the Northwest Territories, Canada. The accuracy of this method is then assessed against reported ice fractions provided by CIS, other segmentation methods, as well as reference data created through visual interpretation of SAR and optical imagery. Specifically, the primary objective of this research is to evaluate the suitability of the IRGS classification method as a means for providing dependable lake ice phenology information using SAR imagery.

1.3 Document Outline

Chapter Two of this document provides background information on lake ice phenology, the use of SAR remote sensing for lake ice monitoring, and a review of the segmentation methodology

used in this study, as well as others. Chapters Three to Five contain the study area, data, and methodology of this study. A discussion of the findings follows in Chapter Six. Chapters Seven and Eight include a conclusion to the findings of this work as well as recommendations for continuation of this research.

2.0 Background

2.1 Lake Ice Phenology

Lake ice phenology, or the annual freeze and thaw cycle of lakes, is a dynamic sequence involving many interacting factors. Local air temperature is the dominant control, but other climatic and non-climatic factors play a role. These factors include precipitation, wind, cloud cover, lake morphometry, elevation, ice albedo, and water inflow from external sources. This section will outline these forces, with a focus on Canadian studies. A short discussion of the recorded changes in lake ice phenology due to climate warming will follow.

Throughout the relevant literature various terms are used to describe the stages of ice growth and decay on lakes. For the sake of simplicity in this document, the following terms will be used to define the stages of the ice season: freeze-up will refer to the period in fall from the first day when ice is detected on a lake surface, to the time of complete ice cover; break-up will refer to the period after which melting begins, up to the point when a lake is free of ice. The 'ice season' will refer to the general period between fall and spring when these processes are taking place.

2.1.1 Freeze-up

As air temperature at the site of a lake drops in the fall, mixing occurs between surface and deeper waters due to temperature dependent variations in density. This continues until the entire water column reaches maximum density at 4°C (Ragotzkie, 1978). The time it takes for this to occur is largely a product of the capacity for heat storage within a lake, with large deep lakes freezing later than smaller, shallower lakes under similar conditions (Williams, 1965). Surface waters continue to cool and a stable water layer forms as it approaches the freezing point,

producing the initial ice layer. This fragile layer called skim ice generally appears first along the calm edges of lakes and in bays protected from wind (Jeffries et al., 2005). Wind can play a role in the timing of freeze-up as it increases the rate of mixing, speeding the cooling process (Williams, 1965). The average bulk temperature a lake needs to reach in order to freeze at the surface has been related to the fetch of the lake and amount of wind present. Jeffries et al. (2005) report that smaller lakes begin to freeze at bulk temperatures of 2-3°C whereas larger lakes need to reach 1°C in order for freeze-up to begin. In addition, initial ice must reach a certain thickness on large lakes in order to resist breaking so a complete cover of ice can form. Jones (1969) also suggests that snow fall may hasten ice growth during this time, as it provides freezing nuclei when it falls on open water. Frazil ice may also appear during freeze-up. This is a collection of loose ice crystals formed under turbulent or windy conditions, appearing similar to slush on the lake surface. Both of these initial types of ice can integrate into the solid ice cover later in the season (Jeffries et al., 2012).

Two types of thicker ice dominate on lakes throughout the ice season. The first is congelation ice which forms at the ice-water interface as water freezes to the bottom of the initial ice layer. This type of ice is often called black ice as it lacks texture and has a clear appearance (Jeffries et al., 2012). The second is white ice, named for its high light scattering and albedo. White ice forms when snow cover is present on pre-formed ice and can be produced in two ways. The first occurs when the weight of the snow load overcomes the buoyancy of the ice sheet below, causing flooding at the snow-ice interface and the creation of slush. Rapid freezing then takes place to form a white ice layer (Ashton, 2011). The second process occurs when meltwater or rain percolates down through snow to the top of the ice sheet and later freezes (Bengtsson, 1986). In many cases wind causes snow to accumulate close to the shorelines of lakes throughout ice cover duration, meaning

white ice is observed more extensively in these areas whereas bare, black ice is more common in the center of a lake (Bengtsson, 1986). An example of how black and white ice appear in a SAR scene is shown in Figure 2.2.2.

Local air temperature has been shown to be the most influential factor determining the timing of freeze-up as well as break-up. Although lake ice phenology is influenced by many factors, heat loss or gain at the surface due to temperature conditions is the governing force (Williams, 1965). Duguay et al. (2006) confirmed this in a Canada-wide time series study from 1966-1995. The authors reported that the arrival of the autumn or spring 0°C isotherm date strongly related the timing of freeze-up and break-up, but that these events lagged one to four weeks behind the 0°C isotherm date. Similar findings are reported by Williams et al. (2004), Ghanbari et al. (2009), and Palecki & Barry (1986).

Several other factors may influence the process of freeze-up and length of the ice season. Patterns in large scale atmosphere and ocean circulation known as teleconnections are related to trends in air temperature throughout northern landscapes, and have been related to variations in lake ice phenology (Bonsal et al., 2006). Bonsal et al. (2006) examined the relationship between some of these indices and freshwater ice duration over Canada from 1950-1999. El Nino/ Southern Oscillation as well as the positive phases of the Pacific Decadal Oscillation and the Pacific North American pattern were found to be linked with shorter ice cover duration for most of Northwestern North America. These patterns are associated with a deeper Aleutian low which allows an increase of relatively warmer Pacific air into the Northwest (Prowse et al., 2011b). These results are congruent with an earlier study by Robertson et al. (2000) who connected the climatic impacts of El Niño with lake and river ice phenology events in the Northern Hemisphere between 1900 and 1995.

The presence of snow cover has also been described as a driver for ice thickening due to the role it plays in white ice formation. As mentioned, when the weight of a snow cover overcomes the buoyancy of the ice layer below, a slushing event occurs resulting in the creation of a white ice layer (Adams & Roulet, 1980; Ashton, 2011). In addition to this cycle, the decrease in dry snow cover after a slushing event later leads to additional ice thickening (Ashton, 2011). This supports the acceptance that snow acts as insulation, hindering the growth of underlying ice because of its relatively low thermal conductivity (Duguay et al., 2003). A study by Rouse et al. (2008) corroborate this through their presentation of ice thickness models for 3 meter and 30 meter deep lakes across the Mackenzie River delta, under both full snow and no snow conditions. The modeled images clearly demonstrate the insulating effects of snow cover in relation to ice thickness, where maximum ice thickness on bare ice reaches 2 meters, while under snow cover only reaches 1.4 meters. This is mildly supported by Williams et al. (2004) who related snow depth to ice thickness in a survey of 143 lakes across North America, but reported only a slight decrease in ice thickness as snow depth increased. In this case the single-date measurement used for each may not have represented conditions throughout the season, causing the weakly observed correlation.

The presence or absence of clouds has also been linked to ice growth. Curry et al. (1993) modeled the effects of cloud cover in the high Arctic and reported that, especially during polar darkness, the absence of clouds increased the loss of long wave radiation and enhanced ice growth. Brown & Duguay (2010) summarize that clouds can both trap long wave radiation slowing ice growth, or reflect solar radiation away from the ice cover either enhancing ice growth or slowing spring melt depending on the season.

2.1.2 Break-up

As previously mentioned, air temperature is the main control determining the onset of break-up, with this event taking place one to four weeks after the 0°C isotherm date depending on the size of the lake (Duguay et al., 2006). Spring break-up has been established to be more sensitive to changes in air temperature than freeze-up even though both follow closely with seasonal temperature trends. Duguay et al. (2006) observed earlier break up at various locations as a result of climate warming, but did not deduce a significant change in the timing of freeze-up. This is in agreement with a previous examination by Schindler et al. (1990) who reported a decrease in ice cover duration due to earlier spring break-up by about 20 days over a 20 year time series in Northwestern Ontario.

As with freeze-up, several other factors may play a role during the melt season. The albedo of ice cover plays a major role in the speed of break-up and is determined by the type of ice, its density, and presence of snow. Very dense ice has the lowest albedo, and this increases as density decreases, such as in the case of white ice (Heron & Woo, 1994). Jones (1969) observes that the presence of white ice delays melting, and suggests that the distribution of white ice is more important during break-up than the thickness if the ice cover. Snow can protect underlying ice from melting as it inhibits heat transfer from the atmosphere and reflects incoming solar radiation (Brown & Duguay, 2010). Albedo is highest when there is fresh snow present on the ice, and decreases during melt as small ponds are formed (Brown & Duguay, 2010). As this continues, solar radiation absorption increases and brings about the onset of a positive feedback loop. This weakening of the ice cover makes it vulnerable to mechanical disintegration from wind and turbulence, resulting in further melting (Palecki & Barry, 1986).

Inflowing water from either land runoff or rivers can effect both freeze-up and break-up as it introduces relatively warm water and creates turbulence (Brown & Duguay, 2010). This is recorded in a study on variations in ice phenology on Great Slave Lake by Howell et al. (2009). The authors observe that the central body of the lake is the first area clear of ice and also has the shortest melt period because of inflow from the Slave River.

The elevation of a lake has also been shown to have some effect on the timing of ice phenology events, where generally higher altitude lakes experience longer ice cover duration than those in the same region at lower altitudes (Brown & Duguay, 2010). Livingstone (2010) investigated ice phenology events on high elevation lakes in the Tatra Mountains, Poland. Lake elevations ranged from 1,580 to 2,157 meters above sea level and a clear dependence on altitude was recorded, with ice cover duration increasing by 10.2 days per 100 m. Break-up timing was especially found to correlate strongly with changes in elevation, the highest lakes thawing almost 50 days later than the lowest ones (Livingstone et al., 2010).

When considering the many factors at play in the freeze-up and break-up of ice cover on lakes it is clear that the process is dynamic and complex. Lake ice phenology incorporates both climatic and non-climatic factors which influence ice cover duration and thickness. Although air temperature plays the largest role during this process, smaller factors may cause yearly variations in phenology at a given site. Factors such as rain and snowfall during this cycle may become increasingly important as climate normals continue to shift, deepening the need for high quality lake ice cover monitoring.

2.1.3 Trends in Lake Ice Phenology

The timing and duration of lake ice cover has been demonstrated as a powerful indicator of climate change and variability in several studies including those by Duguay et al. (2003), Magnuson (2000), Livingstone (1997), and Palecki & Barry (1986). These analyses as well as others have indicated that climate warming is responsible for changes to the timing of lake ice phenology events. Specifically, long term historical records have demonstrated the relationship between shortened ice cover duration, earlier break-up dates, and the increase in global mean air temperature since the industrial revolution (Duguay et al., 2006; Livingstone et al., 2010). Observed and projected effects that this may have on infrastructure, aquatic habitat, permafrost, and other components of the natural and built environment are summarized by Prowse et al. (2011a).

As it has been mentioned, the timing of break-up is more affected by rising air temperatures than freeze-up. A study of historical trends in freshwater ice conducted by Magnuson (2000) revealed that there is strong evidence showing earlier ice break-up and later freeze-up throughout the Northern Hemisphere. In this 150 year study the author calculated changes in freeze-up averaging 5.8 days later per hundred years, and break-up averaging 6.5 days earlier per hundred years. This study also revealed that since the 1950s inter-annual variation in the timing of phenology events has increased. Variability was recorded as 12% higher during freeze-up and 5% higher during break-up than the previous period (Magnuson, 2000). Brown & Duguay (2011) simulated lake ice phenology across the Arctic regions of North America using the Canadian Lake Ice Model (CLIMo) for a 139 year period up to 2100. This model calculated mean trends from 2041-2070 revealing a 10-25 day reduction in ice cover duration for shallow lakes, and a 10-30

day reduction for deeper lakes. They concluded that changes in air temperature and precipitation will be responsible for decreases in ice cover duration in the future (Brown & Duguay, 2011).

Ice phenology events on lakes at varying latitudes have been shown to be affected differently by climate change. In a study by Livingstone et al. (2010) the authors revealed that more temperate lakes which already experience a short ice cover will be the most effected by climate warming. This will cause greater decrease in ice cover duration on these lakes, potentially eliminating winter ice cover entirely. This change will have a number of implications for local ecology and climate interactions (Livingstone et al., 2010). These observations confirm the importance of being able to record the coming changes to lake ice cover in a timely, detailed, and reliable way.

2.2 Lake Ice Monitoring with Synthetic Aperture Radar

2.2.1 SAR Remote Sensing

The advancement of SAR remote sensing has allowed for a wealth of lake ice phenology information to be gathered from large and remote expanses. Although optical and thermal sensors are appropriate for this task, SAR imaging systems have become the standard tool for operational ice cover monitoring because of their capability to capture images in polar darkness and through any cloud cover conditions.

SAR imagers are active microwave sensors which operate through the transmission and reception of microwave electromagnetic (EM) energy. A timed pulse of energy is generated and focused through the antenna of the sensor toward the target in question. The reflected or 'backscattered' energy is then returned to the sensor and detected by the same antenna. Early imaging radar systems aboard aircraft used real aperture radar (RAR), however the spatial resolution along the azimuth direction was very coarse (Figure 2.2.1) (Shokr & Sinha, 2015).

Azimuth resolution of a system is a direct function of its antenna length, with a longer antenna resulting in better resolution. For RAR the required antenna length to achieve reasonable resolution from a satellite system is not possible. SAR overcomes this problem as it allows for a long antenna to be synthesized through Doppler-effect signal processing (Kellndorfer & McDonald, 2009).

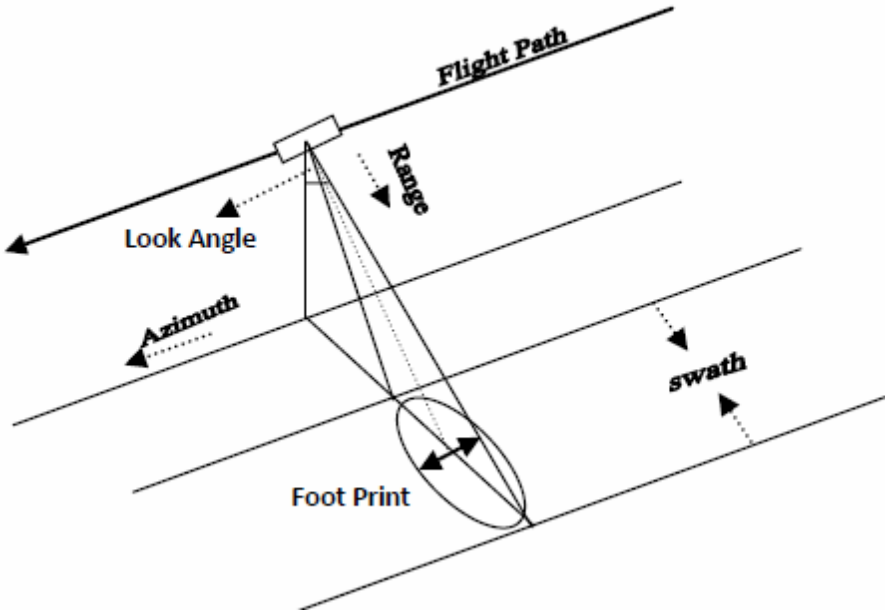

Figure 2.2.1 SAR geometry (Ray et al, 2015).

The frequency or wavelength of the EM pulse sent by a SAR system governs the properties which are best observed by the system. RADARSAT and RADARSAT-2 operate in C band (at 5.6cm wavelength) as this has been determined a suitable wavelength for monitoring ice, however other wavelengths such as X band are also used for sea and lake ice monitoring (Holmes, 1984; Sobiech & Dierking, 2013). Polarization describes how an EM wave propagates along an invisible plane as it travels to and from a target. SAR systems predominantly transmit energy and receive backscatter in the horizontal or vertical polarization (relative to the surface or the earth), however coming missions will carry fully polarimetric or compact polarimetric sensors which allow for additional signatures other than backscatter to be derived (Kellndorfer & McDonald, 2009).

The amount of backscattering received to a SAR system depends on the effect that a ground target will have on the transmitted pulse. This parameter is called the backscatter coefficient or 'sigma naught' (σ^0) and can be treated as a property of the target surface in question. The value of σ^0 is presented in decibels (dB) and is determined by surface roughness as well as the physical and electrical properties of the target. The parameters of a SAR system including wavelength, polarization, and incidence angle also have an effect on σ^0 value (Shokr & Sinha, 2015).

The CIS heavily relies on SAR imagery to allow for operational sea ice and lake ice monitoring. Trained ice analysts use SAR as well as optical images along with ancillary data such as weather information and recent ice conditions to create daily ice charts for Canada's northern and eastern marine coasts as well as for the Laurentian Great Lakes. CIS also uses this information to monitor ice cover on over 130 inland lakes. The amount of ice cover on these lakes is recorded as a fraction out of ten on a weekly basis. This information is used by the Canadian Meteorological Centre (CMC) for use in weather forecasting models. RADARSAT-2 has provided the CIS with SAR images which improve on the previously launched RADARSAT mission through the inclusion of both HH and HV polarized images available in the ScanSAR Wide mode which offers a swath width of 500km. The upcoming RADARSAT Constellation Mission will be outfitted to deliver compact polarimetric information in its wide swath modes (Dabboor & Geldsetzer, 2014). The recently launched Sentinel-1A and B satellites also provide C band SAR imagery to CIS in multiple polarizations in a wide swath mode.

2.2.2 Challenges

Unsupervised classification of ice and open water on a lake requires an algorithm to be able to differentiate between these two classes. This matter is complicated by the fact that SAR backscatter

signatures of ice and water vary significantly throughout and across scenes, where several signatures can be observed for each class (Geldsetzer & van der Sanden, 2013). In the beginning of the ice season, congelation ice appears dark (Figure 2.2.2b). This occurs because the radar signal is scattered away from the sensor off of the basal ice-water interface due to the differences in dielectric constants between ice (ε'_I = 2.2 to 4.5) and water (ε'_W = 80) (Duguay et al., 2002). This causes confusion with open water as there is a low σ^0 contrast between dark open water and newly formed ice. Later in the season backscatter increases due to further thickening of the ice, as well as increased roughness from cracking and deformation (Morris et al., 1995). Snow ice results in volume scattering and a bright backscatter throughout the ice season (Duguay et al., 2002).

During spring melt the presence of water on the ice surface from ice or snow cover melt causes a decrease in σ^0 value because of increased specular scattering. When this melt water drains a rough ice surface is often left behind causing another spike in backscatter values (Surdu et al., 2015). Open water, which commonly appears very dark in SAR scenes can appear brighter a result of surface roughness caused by wind (Geldsetzer et al., 2010).

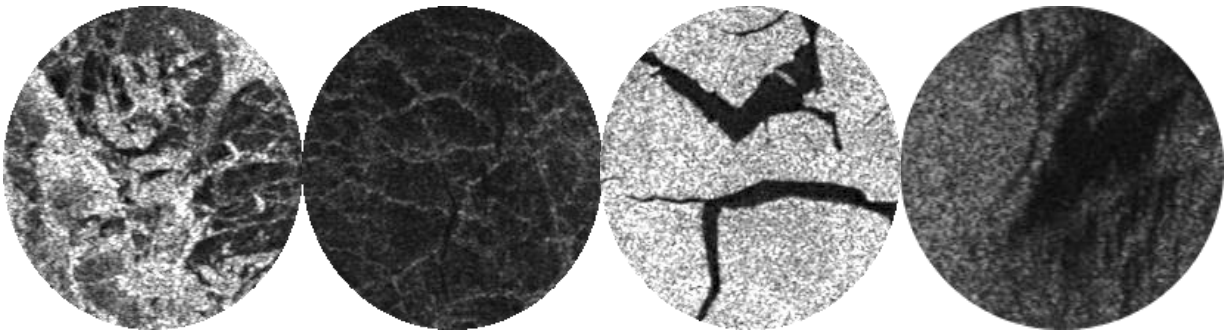

(a) (b) (c) (d)

Figure 2.2.2 Samples of backscatter signatures of ice and water in RADARSAT-2 SAR scenes. (a) mix of deformed white and black ice, (b) black ice, (c) white ice during spring melt with open water leads, (d) wind effect on open water.

In addition to these complications, variation in incidence angle across large swath SAR scenes causes discrepancies in all backscatter signatures; ice which appears very dark in the far range may appear brighter in the near range even though they are the same age and type. Because of these similarities, highly accurate automated classification of ice and water classes is made difficult.

Acquiring multiple polarizations of a scene provides additional information which can be used to increase the performance of classification methods. Information captured in the HV polarization is less affected by variations in incidence angle and strong wind even when large areas of open water are present. This results in a more consistently low σ^0 value from open water, but the tradeoff for this is a reduced contrast between water and ice, especially new thin ice (Surdu et al., 2015). For this reason, dual polarization imagery is beneficial to use during classification as compared to single polarization data.

2.3 Ice-Water Segmentation and Classification

2.3.1 Previous Approaches

Segmentation methods split an image into a set number of classes containing uniform information. These methods are widely used to interpret remotely sensed data, with simple techniques included in various GIS and image processing packages such as ArcMap and ENVI. The task of classification goes a step further by assigning a meaningful label to each segmented class (ex. ice and water). The need for a way to quickly and reliably interpret SAR images of ice and water has motivated a library of work over the past three decades. Publications have employed many standard and novel approaches for classification in marine bodies, with some applications to freshwater lakes and rivers. Unsupervised and semi-supervised approaches including threshold, clustering, support vector machines, and others have been explored, with researchers often

combining several methods and data sources into a multi-step workflow. A sample of studies are discussed here, with a focus on those which employ C band SAR data for research over ice and water.

Threshold methods have been explored in several ice segmentation studies. This method can be useful for separating objects that exist on a contrasting background like ice on water. In simple thresholding all pixels at or above a predefined grey level value are assigned to one class, and all those below the 'cut-off' fall into the other (Castleman, 1996). Thresholding may be done globally in an image wherein the cut-off value remains constant, or may be done locally where an image is subdivided and has a cut-off value chosen for each region based on its unique properties (Castleman, 1996). A dynamic local thresholding technique was introduced by Haverkamp et al. (1993) specifically adapted for sea ice segmentation and was found to be more accurate than previous global thresholding methods. Soh & Tsatsoulis (1999b) furthered this work with the addition of peak detection and spatial clustering. Their approach was tested on more than 300 SAR ice images and subjectively validated by ice analysts from the United States National Ice Center. Despite the local thresholding method the authors reported poor results on images with large areas of open water because of the effects of incidence angle and wind. Later, Geldsetzer et al. (2010) developed a thresholding technique to specifically discriminate between melting lake ice and open water in Radarsat-2 SAR images from Old Crow Flats, Yukon. In this study backscatter thresholds for both HH and HV bands were statistically determined based on grey level metrics, with the HH imagery used to classify initial break-up and HV imagery used later, when 10% or more open water was present. Nghiem & Leshkevich (2007) recorded a comprehensive library of ice backscatter signatures on the Laurentian Great Lakes, and later used this look-up table along with

a simple threshold method to classify open water and several ice types (Leshkevich & Nghiem, 2013).

A watershed algorithm separates segments in a greyscale image by deeming the pixels with the lowest intensity as the bottom of a 'watershed drainage basin' and those with the highest intensity as the ridges which separate these basins. In SAR imagery the algorithm creates many small regions due to the high amount of noise, which then need to be merged. Watershed merging then joins neighboring basins through comparing their average intensities, sizes, and gradients (Clausi et al., 2010, Soh et al., 2004). Soh et al. (2004) build on their previous work, presenting the Advanced Reasoning using Knowledge for Typing of Sea ice (ARKTOS) system, a novel approach for classifying SAR sea ice images. This system incorporated local thresholding, unsupervised clustering, and watershed merging for segmentation, as well as class labeling. The labeling was done through computing attributes from segmented regions and employing a rule-based module to infer the classification labels (Soh et al., 2004). Watershed merging was also incorporated into the IRGS approach (Yu & Clausi, 2007; 2008). In these two works the IRGS methodology is presented, which uses a watershed algorithm to generate a preliminary segmentation. Edge penalties and region growing are also incorporated to produce highly accurate segmentations of RADARSAT images. In their study, Yu & Clausi (2008) found that IRGS produced ice-water segmentation with 97% accuracy. This approach is further explained in the next chapter: 2.3.2 IRGS.

The aim of cluster analysis is to find the natural groupings in a set of unlabeled data based on a quantitative comparison of similarity between the characteristics of data points, with the resulting segmentation having a high level of similarity within a group and low level of similarity between groups (Jain, 2010). Early on, Kwok et al. (1992) used ISODATA clustering to segment SAR sea

ice images of the Canadian arctic and labelled the segments using seasonal look-up tables containing backscatter signatures for several ice types. Weber et al. (2003) applied a fuzzy k-means segmentation (wherein pixels may belong to more than one group) to RADARSAT images of the Peace River, Alberta in order to classify major ice cover types, and concluded that the outcomes appeared accurate when compared to visual interpretation and airborne observations. *k* -means clustering was also employed by Sobiech & Dierking (2013) to perform ice-water segmentation during spring break-up on small lakes in the Lena Delta, Siberia. Their results demonstrated that this method is suitable for segmentation, though it should be noted that backscatter values on the small lakes studied were not affected by incidence angle or wind. Further advances by Gauthier et al. (2010) combined image texture information with a fuzzy k-means algorithm to allow for automated segmentation of ice classes and open water in RADARSAT images of rivers in northern Quebec. The authors reported overall accuracy up to 76% when results were validated against ground photos, aerial surveys, and field measurements.

Since ice and water can often have similar backscatter signatures in a SAR scene, texture within an image is important to consider in order to increase the accuracy of classification results. In a SAR image this means quantifying the nature of grey level variation between a set of items in a scene, for example ice floes (Castleman, 1996). This is often done using grey level co-occurrence matrices (GLCM) which represent the relationship and distance between neighboring pixels. The use of texture features for sea ice classification was introduced by Holmes et al. (1984) who computed two textural images (entropy and inertia) using GLCM for a high resolution X-band HV image of the Beaufort Sea. The authors reported an overall accuracy of 65%, recommending that future work incorporate additional texture features such as uniformity and correlation. Gill (2003) derived textural and statistical image products from RADARSAT images and used them to classify

sea ice and water with a fuzzy screening method. Karvonen et al. (2005) developed an algorithm for ice-water discrimination also using RADARSAT images. The authors did not use GLCM, but instead computed segment-wise autocorrelation as a texture measure as they found it was not sensitive to wave conditions or variations in incidence angle. Zakhvatkina et al. (2013) later investigated which GLCM SAR image texture features were optimal for discriminating between sea ice types in ENVISAT ASAR imagery. The authors calculated nine texture features and used them to train a neural network classifier which was then tested on 20 images, resulting in average classification accuracy greater than 80%.

Support vector machines (SVM) have recently been used for both segmenting and labelling SAR images of ice and water. The SVM method involves the construction of a decision boundary in the feature space of data based on the properties of training samples. This boundary can then be used to segment classes or allocate labels for the classes in question (Tso, 2001). An SVM model which used backscatter and texture features to assign ice-water labels after segmentation was employed by Leigh et al (2014) for use with IRGS segmentation, and was found to be up to 97% accurate when tested on 20 scenes. Liu et al. (2015) presented an approach which used backscatter and texture information from RADARSAT-2 images as well as ice concentration for SVM classification. First, an initial SVM was carried out using 10 backscatter and texture bands as input, and the result was used to extract ice concentration. Another SVM was then implemented using the original 10 bands as well as concentration as input. The final result was then labelled into multiple sea ice types using a decision tree technique. The authors reasoned that ice concentration is a characteristic of ice types and thus should be exploited during classification, for example old ice often has high concentrations because several large ice floes are connected across an area (Liu et al., 2015). Zakhvatkina et al. (2017) also used an SVM algorithm trained with backscatter and

texture features from manually classified images. Their fully automated technique was used to process over 2700 RADARSAT-2 scenes of Arctic sea ice and water. The authors noted a high level of correspondence between manually classified images, ice charts, and the algorithm results, reporting an average total accuracy of 91%.

Many groups have offered solutions to the problem of classifying ice and water in SAR images, incorporating clustering approaches, watershed merging, texture information, and SVM classifiers to produce reliable results. The VIP lab at the University of Waterloo has developed the novel MAGIC user interface for this purpose. It houses the aforementioned IRGS algorithm as well as other standard segmentation techniques including *k*-means and Gaussian mixture model (GMM). These methods are employed in this study, and thus are further explained in the following sections.

2.3.2 IRGS Segmentation

The IRGS algorithm has been created to perform segmentation and ultimately classification of SAR ice imagery in a in an automated and reliable way. This technique, which combines aspects of several image processing methods, is the product of over 15 years of investigation by students and researchers. This work has been united and packaged in the MAGIC system. *K*-means and GMM segmentation approaches are included in the MAGIC user interface and these will be measured against IRGS in this study.

The IRGS algorithm has been specifically tailored to deal with the unique segmentation challenges present in SAR scenes of ice and water. The steps involved in the IRGS approach are outlined in Figure 2.3.1. When employing IRGS the region of interest is first divided into a number of sub-regions called ‘autopolygons’ using the HV image as input (Figure 2.3.1b). These are generated through a watershed segmentation creating regions which follow the natural structure of

the image (Vincent & Soille, 1991; Leigh et al., 2014). This step is carried out using only the HV image because it shows less backscatter variation as a result of strong wind or incidence angle

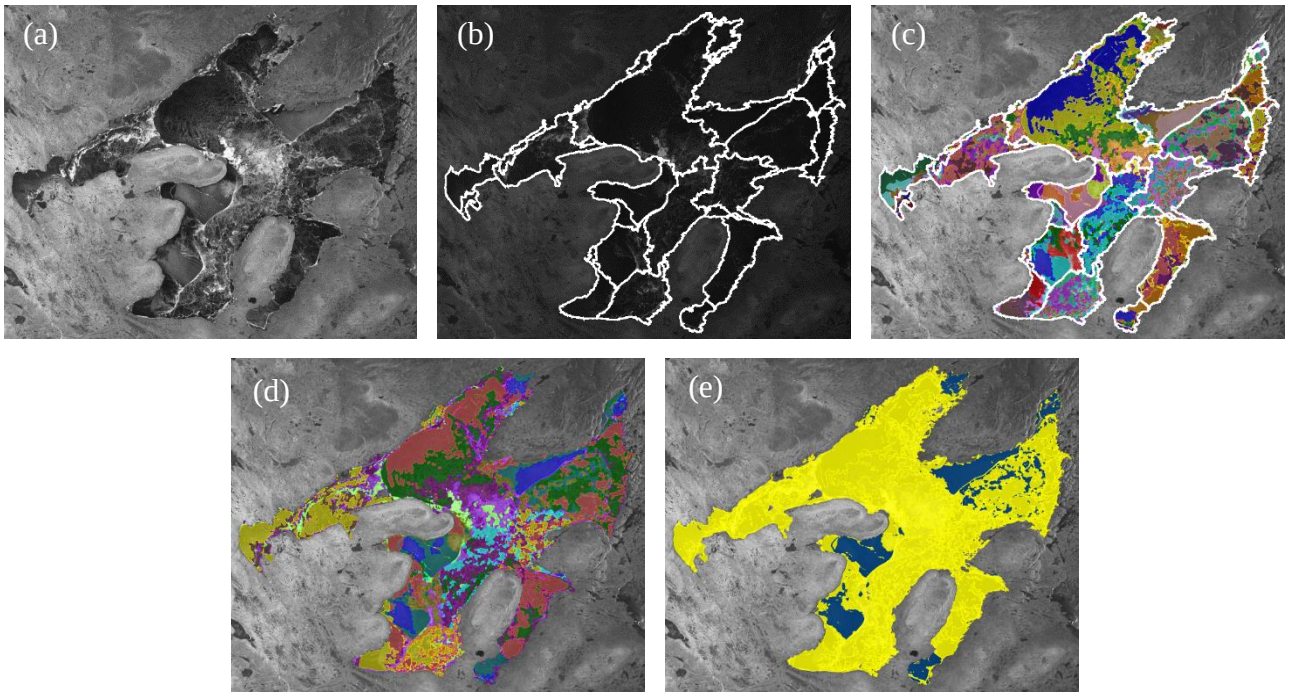

Figure 2.3.1 Steps of the IRGS segmentation approach. (a) HH polarization SAR image, (b) HV image after autopolygon segmentation, (c) local IRGS segmentation within each autopolygon, (d) all segments 'glued' into the final chosen number of classes, (e) final segmentation after manual labelling where yellow represents ice and blue represents open water.

effects. The autopolygons are meant to decrease errors caused by these effects across an image, as each autopolygon is segmented individually in the following step.

Within each autopolygon, small uniform regions are distinguished again using a watershed algorithm. Each watershed region is then represented by a node in a region adjacency graph and assigned an initial label (Yu et al., 2012). The subsequent segmentation is an iterative process which involves merging and clustering regions towards an ideal configuration with fewer nodes (Clausi et al., 2010; Yu et al., 2012). During this process edge strength between adjacent regions as well as neighborhood information is also considered, increasing segmentation accuracy (Yu &

Clausi, 2007). This process ultimately breaks up each autopolygon into homogenous regions of either ice or water. Once complete, image wide 'gluing' is performed, which merges similar regions from any of the autopolygons into a set number of final classes as defined by the user, again using edge strength and neighborhood information. This is called the 'Glocal' approach as it incorporates 'high detail local' and 'large scale global' information (Leigh et al., 2014). These final classes can then be labeled manually by the user, or labeled through the use of an unsupervised technique such as an SVM following the work of Leigh et al. (2014).

Recent work by Li et al. (2015) used some properties of IRGS as well as incorporated self-training in a semi-supervised approach for ice-water classification. In addition, Wang et al. (2016) combined ice/water information produced in MAGIC with AMSR-E ice concentration data to generate improved ice concentration estimates.

2.3.3 *K*-Means and Gaussian Mixture Model Segmentation

Unsupervised *k*-means segmentation has been employed in a number of cases to separate various ice types and open water on lakes and rivers in SAR scenes, making it a well-known method to compare to the IRGS segmentation approach. Both the *k*-means and GMM segmentation algorithms are partitional squared error clustering methods which are standard in pattern-recognition. The process of segmentation begins with the user choosing a fixed number of classes (*k*) to be assigned to the image. The algorithm then chooses *k* cluster centers to coincide with randomly chosen values in the image. Each other value is then assigned to the most similar cluster center in order to form the initial classes. The means of these classes are then computed and become the new cluster centers, and initial class members are then reassigned based on these new cluster centers. In GMM segmentation both the means and the covariances of the initial classes are

computed to select the new cluster center. The last two steps are repeated until there is minimal reassignment, and the sum of the distance between the values in a class and the cluster center for that class is as small as possible. The algorithm also ends if a maximum number of iterations set by the user is reached (Jain et al., 1999). Although it was first proposed more than half a century ago, *k*-means clustering remains as one of the most widely used algorithms of its type, due to its efficiency and high rate of success in many instances (Jain, 2010).

A major downfall of these techniques is that the algorithm is sensitive to the partition of the initial cluster centers. Essentially, when the initial cluster centers are chosen the segmentation is stuck with them to some degree, the even if they do not best represent the natural groupings of the image values (Jain et al., 1999).

3.0 Study Area

The images used in this study are captured over GBL and GSL, shown in Figure 3.0.1. GBL and GSL are both deep, large lakes located within the Mackenzie River basin, Northwest Territories. GBL spans ~31,000km^2 with a mean depth of 76m and a maximum depth of 446m. It is described to be ice covered from late November to July (Howell et al., 2009). Mean monthly temperatures at Déline range from 13.3 to -25.2°C, remaining below 0°C from October to April as shown in Figure 3.0.2.

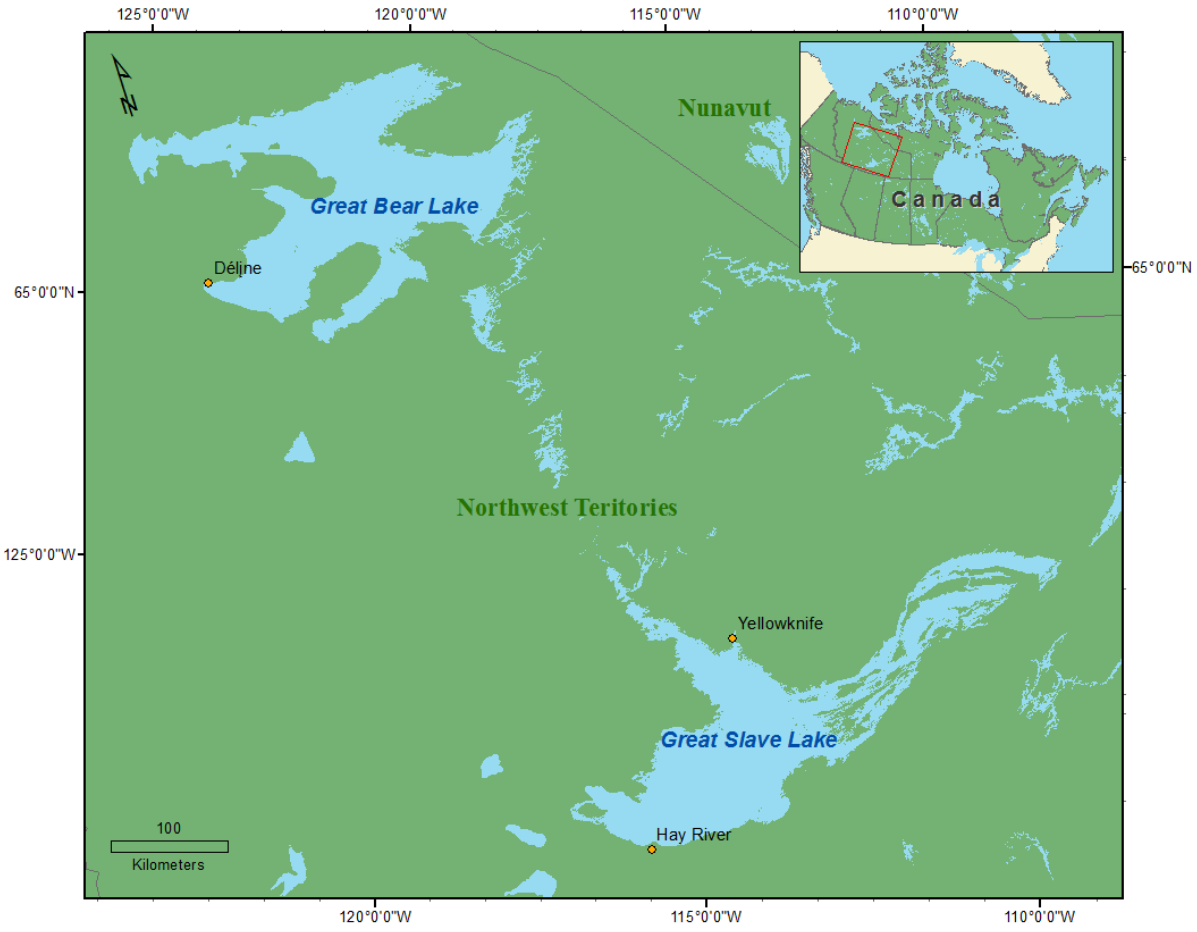

Figure 3.0.2.3.1 Location of Great Bear Lake and Great Slave Lake within Canada. Climate information is available from stations located in Déline, Hay River, and Yellowknife.

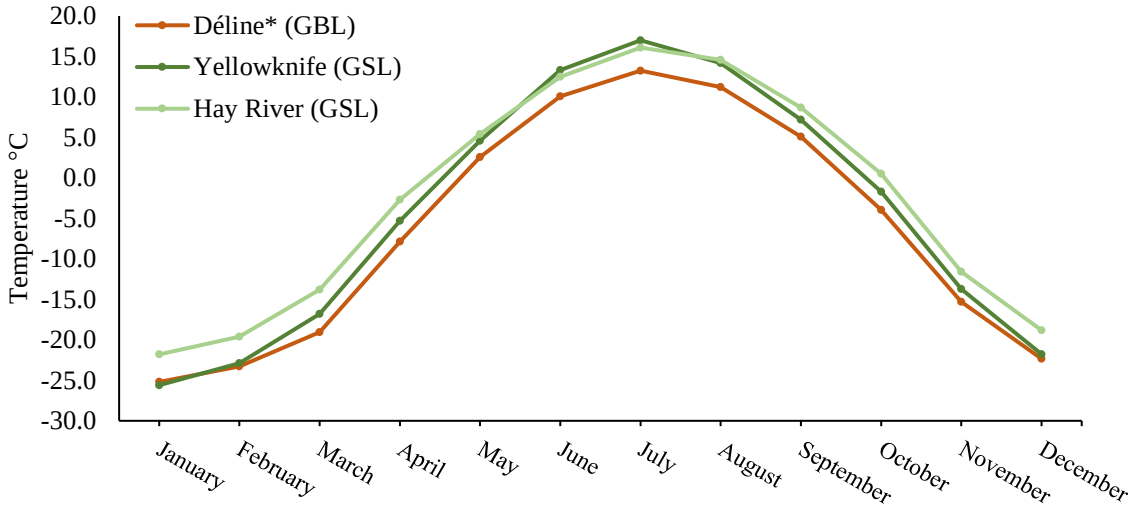

Figure 3.0.2 Mean monthly temperature normals for 1981-2010 at Délene, Yellowknife, and Hay River climate stations near Great Bear Lake and Great Slave Lake. Temperature Data from Environment Canada (climate.weather.gc.ca). *Déline normals calculated with mean monthly temperatures from 1991-2010 only, based on available data.

GSL spans an area of ~27,000km^2 with the central basin averaging 41m in depth with a maximum of 163m, while the much deeper east arm of the lake averages 249m in depth, reaching a maximum of 614m. At a lower latitude, GSL is generally ice covered between late December and early June (Howell et al., 2009). Temperatures recorded at Yellowknife and Hay River near GSL are slightly warmer than those observed at Déline, ranging from 17 to -25.6°C and 16.1 to -21.8°C respectively (see Figure 3.0.2).

4.0 Data

Sixty-one RADARSAT-2 scenes of GBL or GSL are used in this study spanning the winters of 2013-2016 as outlined in Tables 6.1.2 and 6.1.3. In total, three ice cover seasons are included. All images are dual-polarized HH and HV images in ScanSAR Wide beam mode. Each image covers a swath width of 500 by 500 km, with a nominal spatial resolution of 100 m. Each image is approximately 10,000 by 10,000 pixels with 50 m by 50 m pixel spacing. Images were acquired in both ascending and descending passes, with incidence angles of 20-49 degrees in each scene (MacDonald, Dettwiler and Associates Ltd., 2014). The percent of the lake covered by the SAR scene is also recorded in Tables 6.1.2 and 6.1.3 as this can be a source of variance between the classification outcomes and the CIS weekly fraction. Only scenes which included 70% or more of the target lake were used in this study. It should also be noted that scenes where a lake was completely ice covered or completely open water were excluded. The chosen image set represents a suitable sample for this study as it offers a range of backscatter signatures and incidence angles for ice and water at varying points throughout freeze-up and break-up process.

Weekly ice concentration fractions are recorded by CIS for two sections (north and south) for both GBL and GSL as shown in Figure 4.1. For the sake of simplicity when reporting the results of this study these fractions have been averaged for each lake. The fraction most closely corresponding to the timing of each scene is outlined in Tables 6.1.2 and 6.1.3. During freeze-up, the notation of 9+ describes a lake which is more than 9/10ths ice covered or is completely ice covered but may continue to change fraction. This notation reports within CIS that imagery of this lake should continue to be ordered in case ice coverage changes in the coming weeks. During spring break-up the 9+ fraction signifies a lake that has begun the process of break-up but is still

more than 9/10ths ice covered (V. Pinard, personal communication, 2018). These CIS ice fractions are used to compare to the total ice concentration produced by IRGS, *k*-means, and GMM segmentation methods.

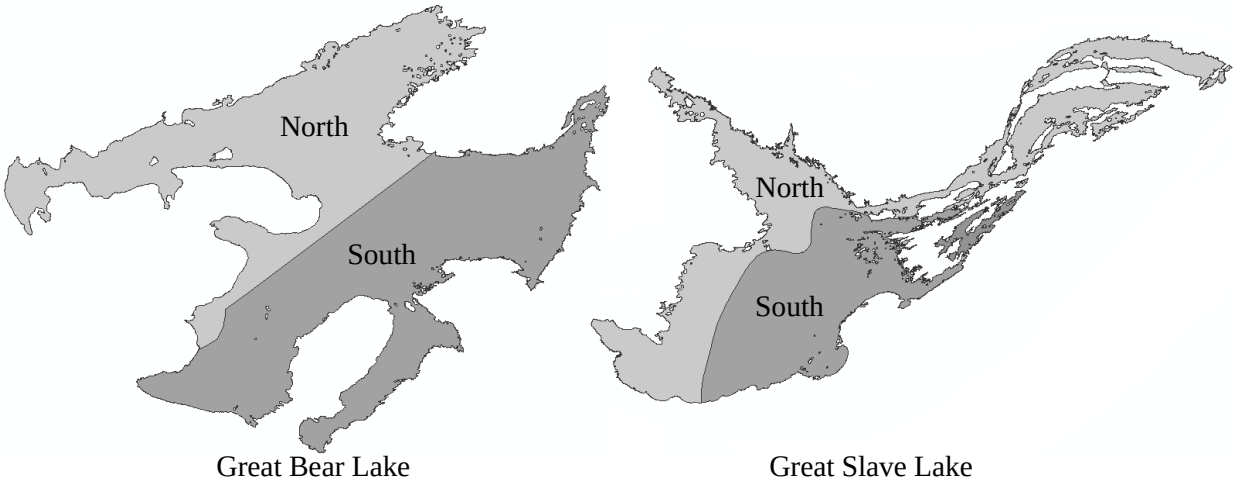

Figure 2.3.1 Delineation of north and south sections of GBL and GSL as provided by CIS.

Temperature information was taken into account during the creation of reference data as well as during validation. Climate stations in Déline, Hay River, and Yellowknife (Figure 3.0.1) provided daily climate information up to 2016. Temperature recorded at the Déline station was used for comparison to results at GBL, whereas the temperatures from Hay River and Yellowknife were averaged to compare with results at GSL.

Terra and Aqua satellite MODIS (Moderate Resolution Imaging Spectroradiometer) optical imagery is also employed in this study. This imagery was used to provide clarity during the creation of reference data as well as for visual evaluation of the classification outcomes, however availability was limited by cloud cover. Imagery was accessed through the Worldview web platform made available by NASA (earthdata.nasa.gov/labs/worldview). These reference images generated an understanding of the evolution of freeze-up and break-up on GSL and GBL during

the study periods, and were necessary for accurate interpretation of the SAR scenes used in this study.

As mentioned, an automated classification workflow for monitoring lake ice is required to be fast in addition to being highly accurate. One way of minimizing computation time is to reduce the size of the images through downsampling. A 4x4 block average creates a new image by taking the average value of every 4 by 4 pixel window to create one pixel, with the outputted image being 1/16th the size of the original. However, this process also reduces image quality which may impact classification results. To test this, a Glocal IRGS classification was conducted for a set of seven images at both full size and after a 4x4 block average and ice concentration was compared to the corresponding CIS ice fraction estimates. At full size the Glocal IRGS process took approximately five minutes, while at reduced size the process took less than thirty seconds. Total ice concentration from the downsampled images closely resembled that from the full size images, as well as closely followed the reported ice fraction from CIS. The average difference in total ice coverage estimates between full size images and downsampled images was 1.8%. From this test, it can be assumed that classification accuracy will not be affected by reduced image size and quality. These results are supported by Leigh et al. (2014) who also used this method when classifying ScanSAR Wide images of sea ice, where the authors reported that downsampling did not affect classification outcomes.

5.0 Methods

5.1 Classification

The MAGIC user interface was used to conduct IRGS, *k*-means, and GMM segmentation for all images in the chosen dataset. Both the co-polarized HH and cross-polarized HV images were used as input for all methods. The north and south sections of each lake (as shown in Figure 4.1) were segmented separately to correspond to the weekly fractions available from CIS, however they were later combined for the sake of simplicity when reporting results. Land and other lakes were excluded from segmentation using mask created through MAGIC using a vector file. A 250 m buffer was added to this mask between the lakes and their shorelines, including islands, in order to minimize the effect that land pixels would have on segmentation outcomes.

Preliminary testing through trial-and-error was conducted to arrive at the suitable parameters to be set for each segmentation method. Although the final results are binary, several separate classes of ice and water resulted from segmentation, and were then labeled as one class or the other. These segmentation classes do not necessarily represent specific ice types, but were needed to minimize areas of ice and water being merged into the same class. For IRGS segmentation, a 12 vertical by 12 horizontal maximum was set for how many autopolygons were to be created per image, these were then automatically generated in MAGIC using a watershed algorithm (see section 2.3.2 for more information). Each autopolygon was then segmented into five initial classes, and these were then 'globally' merged into 12 final classes of either ice or water across the image which were then manually labeled by the user.

For *k*-means and GMM segmentation, images were segmented into 5 final classes. Although this is less than the number of classes for IRGS, it was found that increasing the final number of

classes did not significantly improve the segmentation outcomes. The *k*-means algorithm was applied regionally (based on a watershed) and the GMM algorithm was applied on a pixel-by-pixel basis to add variety to the methods being tested against IRGS. Because these methods are constrained by the partition of the original cluster centers, *k*-means and GMM segmentations for the 2013-2014 year were repeated five times for each scene. Through this test it was revealed that there was a negligible difference between the outcomes of each repetition, so the first outcome was included as the result for these scenes and all others afterward. Other parameters available in MAGIC were left at their default settings.

The parameters chosen for each method remained consistent for the entire dataset. The final classes for each method were then labeled as ice or water by the user and merged, ultimately resulting in a semi-automated binary classification.

5.2 Accuracy Assessment

In order to assess the accuracy of the classification outcomes, reference information was generated by the author for comparison. A random sample of ~400 pixels per image were labelled as either ice or water within MAGIC based on visual interpretation of morphology, texture, and backscatter. A CIS ice analyst provided some training to the author as well as advised the use of an RGB composite of SAR bands (HH/HH/HV) to help discriminate between classes (V. Pinard, personal communication, 2017). This, in addition to MODIS optical imagery was used to help create the most accurate reference pixels possible. In total 24,321 pixels were labeled for the entire dataset of 61 scenes. The reference data was then matched against each classification result image to infer accuracy for each method. This assessment negates the need to create a pixel level ground truth for all scenes in the dataset. The total ice coverage fraction of GBL and GSL for each scene

was also recorded so it could be compared to the reported CIS weekly ice cover fraction. These results are presented in the next chapter.

6.0 Results and Discussion

6.1 Classification Accuracy

Classifications for 61 images of GBL and GSL were carried out in this study using semi-automated IRGS, *k*-means, and GMM methods. The results are compared to CIS weekly fractions of total ice cover as well as reference data created by the author. This is detailed in Tables 6.1.2 and 6.1.3, which document total ice cover fractions and overall accuracy per image for each classification method. Overall error matrices are displayed in Table 6.1.1. These tables show that all of the methods tested performed well, with the Glocal IRGS approach being the most accurate having an overall accuracy of 92.1%. Most errors occurred from ice being misclassified as water for all methods, though this was more prominent in the *k*-means and GMM classifications accounting for 10% and 9% of the totals respectively.

Table 6.1.1 Error matrix totals and percentages by classification method for all GBL and GSL images used in this study. OA is overall average accuracy of the method.

(a) IRGS

		Reference		Classification Totals
		Ice	Water	
Classification	Ice	10308 / 42%	760 / 3%	11068
	Water	1152 / 5%	12101 / 50%	13253
Reference totals		11460	12861	24321
OA	92.1%			

(b) *k*-means

		Reference		Classification Totals
		Ice	Water	
Classification	Ice	8873 / 36%	955 / 4%	9828
	Water	2403 / 10%	12090 / 50%	14493
Reference totals		11276	13045	24321
OA	86.2%			

(c) GMM

		Reference		Classification Totals
		Ice	Water	
Classification	Ice	9217 / 38%	840 / 3%	10057
	Water	2144 / 9%	12120 / 50%	14264
Reference totals		11361	12960	24321
OA	87.7%			

Figure 6.1.1 presents the difference in accuracy between the tested methods as well as between seasons. All methods showed relatively consistent and accurate performance during break-up but had varied performance during freeze-up, with accuracies as low as 67% for IRGS, 56% for *k*-means, and 59% for GMM classifications. When assessing the SAR scenes visually, it is much easier to distinguish ice and water in the break-up images, and because of this it is not surprising that classification results are more accurate during this time.

The IRGS approach performed noticeably better than the other two methods during freeze-up, with an average seasonal accuracy of 89.8%. The freeze-up seasonal accuracies for *k*-means and GMM are 80.9% and 82.4% respectively. Ice error is especially prevalent during freeze-up at 7% for IRGS, 14% for *k*-means, and 13% for GMM. There was no notable difference in the accuracy of methods between scenes of GBL and GSL.

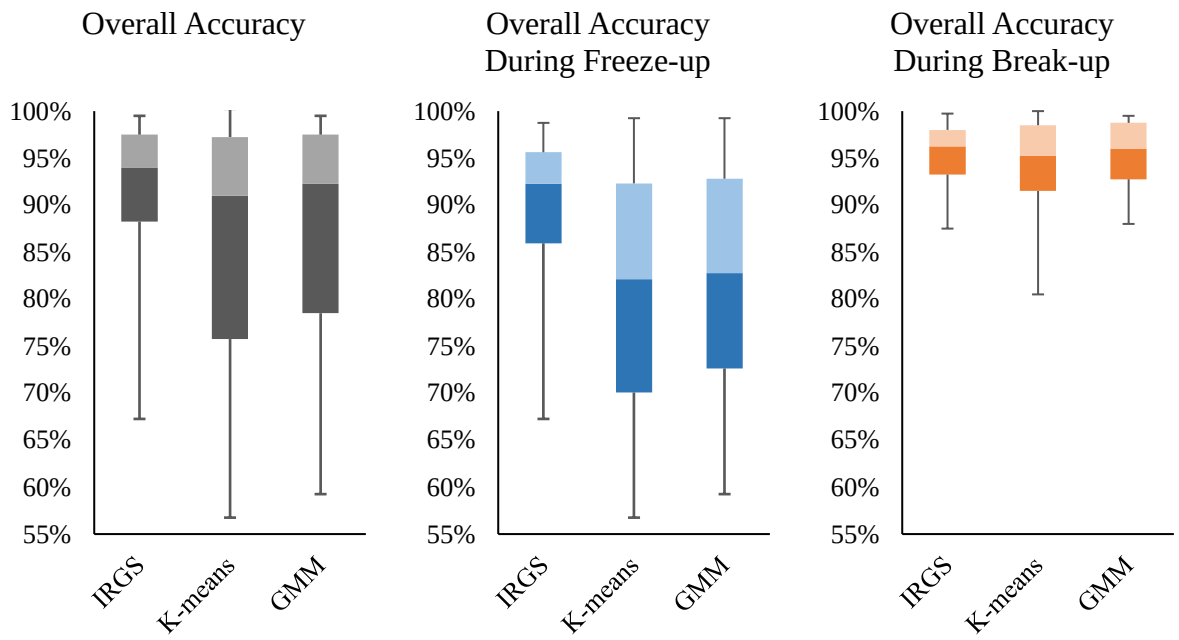

Figure 6.1.1 Box and whisker plots of seasonal and overall accuracy for IRGS, k-means, and GMM classifications for all GBL and GSL images used in this study.

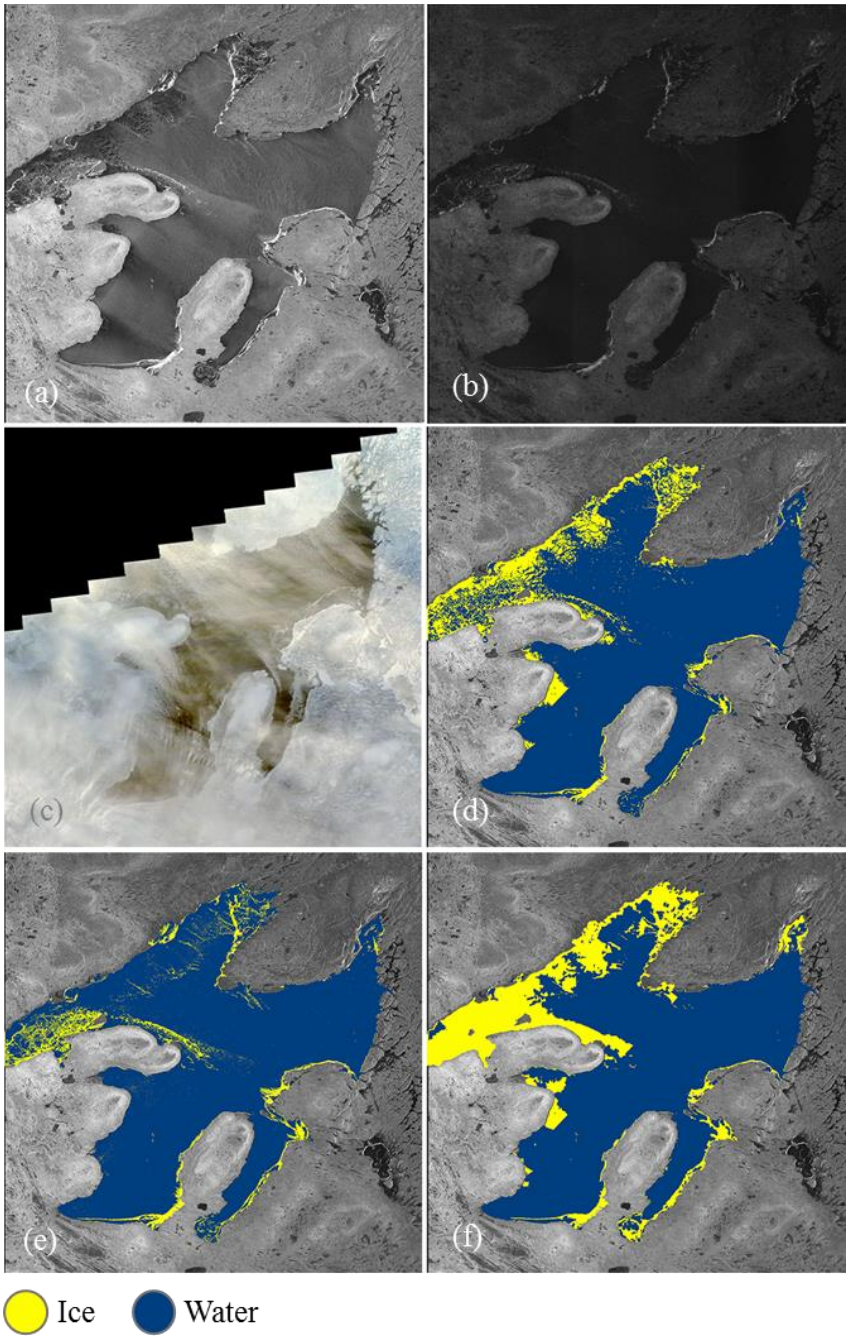

Figure 6.1.2 Classification results for November 19th, 2015 scene of GBL. (a) HH polarized SAR image, (b) HV polarized SAR image, (c) MODIS optical image, (d) k-means classification OA= 84%, (e) GMM classification OA=76%, (f) IRGS classification OA=88%.

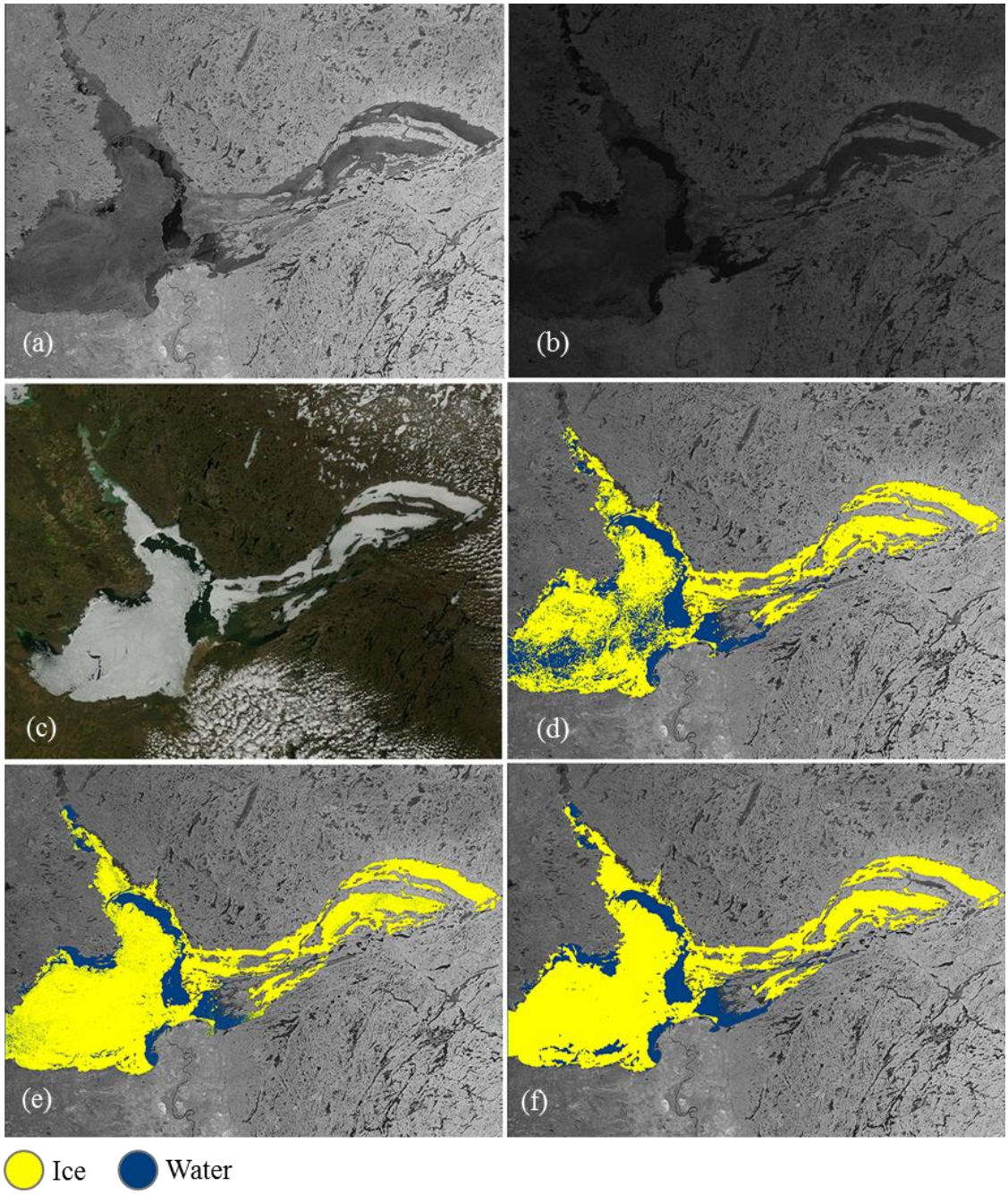

Figure 6.1.3 Classification results for June 5th, 2014 scene of GSL. (a) HH polarized SAR image, (b) HV polarized SAR image, (c) MODIS optical image, (d) k-means classification OA=81%, (e) GMM classification OA=95%, (f) IRGS classification OA=97%.

Figures 6.1.2 and 6.1.3 compare final classification results for all of the tested methods. From these images it is clear that the Glocal IRGS approach provides the most accurate classification of those tested, with most ice and water areas captured correctly. Ice types with low backscatter signatures such as thin black ice were commonly misclassified by the methods used in this study. This is especially evident during freeze-up, where black ice was consistently classified as open water by both the *k*-means and GMM approaches. The IRGS approach adequately captures areas of black ice that are missed by the other approaches, but not completely. This is evidenced in the southernmost arm of GBL in Figure 6.1.2 (f) where black ice is partially but not fully captured by the method.

Figure 6.1.3 shows very good spring break-up results from the IRGS and GMM approaches, however the GMM result shows some speckle noise. This is typical of the GMM results, with other scene outputs from this method containing much more noise than shown here, possibly because this method was executed as pixel-based instead of regionally. All results in this figure have misclassified areas of ice as open water. Surdu et al. (2015) note that the presence of surface water on ice caused by spring melt brings about a decrease in σ^0 value due to increased signal absorption under low wind conditions where surface melt ponds have formed. This may explain why some ice covered areas in the image were classified as open water.

A common error evident in the Glocal IRGS approach arises during the 'gluing' step when homogeneous classes from each autopolygon are merged across the entire scene to create the final class outputs. These classes should remain homogenous during this step, but classes which represent ice and water sometimes end up becoming merged. Figure 6.1.4 displays an example of this issue. In (b) regions of ice shown in pink and violet are separate from the purple water class but in (c) these regions have been merged into one class with water (orange). The resulting

classification after manual labelling then includes regions of ice that have been misclassified as water.

This ‘gluing’ step is necessary to ease manual classification, as the user only needs to label a handful of classes instead of the hundreds present before this step. Unsupervised labelling through the use of an SVM or other method would negate the need for this step and possibly remove this source of error when employing IRGS. Alternatively, texture features could be utilized in this step to decrease this error as they would provide additional information during gluing.

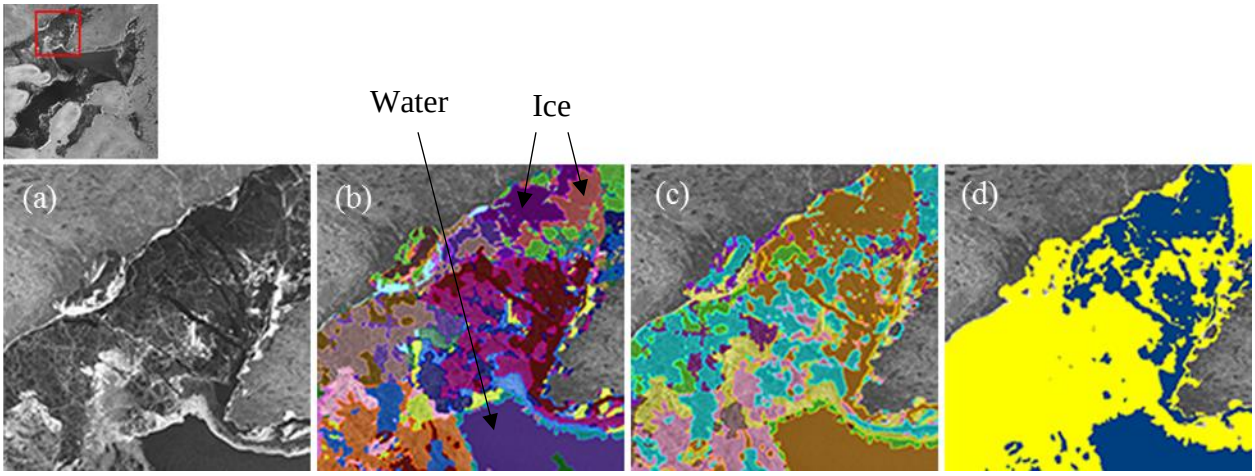

Figure 6.1.4 Example of Glocal merging error evident in the segmentation of a GBL scene. (a) HH polarized SAR image, (b) local segmentation within autopolygons (autopolygons not shown), (c) segmented classes after merging, (d) final classification.

In contrast, Pons Bernad et al. (2009) argue that classification should be done by the user once significant classes are extracted through segmentation. The aim of their study was to create a way to quickly segment images into homogenous regions of interest. These could then be modified by the user. The authors express that in some cases it makes more sense to have a fast and easily executed segmentation algorithm, in combination with an intuitive tool to simplify labeling for the user. This could be applicable in the case of ice-water classification for lake monitoring as there

are already ice analysts available at CIS who could perform this task, however most other recent publications strive for a more automated approach.

Overall, the results demonstrate the ability of the semi-automated Glocal IRGS method to reliably capture the evolution of ice seasons on GBL and GSL. This method provides a visualization of where the ice cover is located during freeze-up and break-up, delivering a very useful product for future studies. As mentioned each Glocal IRGS segmentation took less than 30 seconds, as did the regional *k*-means segmentation. The GMM approach took upwards of 3 minutes for segmentation, likely because it was carried out on a pixel-by-pixel basis instead of regionally, in addition to the extra computational expense inherent in this method. Labelling the final segmentation classes as either ice or water added about 30 seconds to each method.

K-means segmentation is shown to generally produce less accurate classification results when compared to the other methods tested, especially during freeze-up. Although the GMM approach offers a high average accuracy of ~88%, the lengthy run time of this method as well as the visible noise present its results makes it undesirable as an operational method to monitor lake ice phenology. Some errors are present while employing the Glocal IRGS classification, however the high accuracy of ~92% makes it a viable option for monitoring lake ice. The incorporation of unsupervised labelling would be necessary for using this approach operationally in order to expedite the generation of results and minimize errors.

Table 6.1.2 Results of IRGS, *k*-means, and GMM classifications on GBL. Total ice cover fraction as well as overall classification accuracy (OA) are presented. Temperature and percent lake included in the scene are also recorded.

Image ID	Temp (°C)	CIS	# of Samples	IRGS	OA (%)	K-means	OA (%)	GMM	OA (%)	% Lake Included
GBL 11-07-13	-10.9	0.5	394	0.1	98.2	0.3	91.4	0.0	98.0	100
GBL 11-22-13	-22.3	4.0	398	4.1	81.9	3.2	69.1	2.7	68.6	99
GBL 11-29-13	-14.6	4.0	400	3.2	86.8	1.4	74.3	2.1	78.5	96
GBL 12-05-13	-28.2	8.0	400	9.3	98.8	7.6	75.8	7.3	78.5	94
GBL 12-06-13	-21.0	8.0	400	10.0	97.5	10.0	97.5	10.0	97.5	91
GBL 06-12-14	11.8	9+	400	10.0	99.5	10.0	99.5	10.0	99.5	88
GBL 06-19-14	16.3	9+	400	9.7	98.5	9.6	98.5	9.6	98.3	100
GBL 06-29-14	7.1	8.0	400	6.5	92.3	5.8	81.8	6.2	92.3	89
GBL 07-03-14	17.9	2.0	400	2.7	93.3	2.6	93.8	2.1	93.5	96
GBL 07-10-14	12.0	1.0	382	0.1	99.2	0.0	99.2	0.1	99.2	91
GBL 10-31-14	-5.1	0.5	400	0.2	98.3	0.0	98.0	0.1	96.0	96
GBL 11-06-14	-16.6	1.0	400	1.1	92.0	0.9	92.8	1.0	86.8	94
GBL 11-07-14	-20.0	1.0	368	1.4	86.1	0.4	84.2	0.8	86.1	91
GBL 11-12-14	-14.5	1.5	400	1.9	88.5	1.2	83.5	1.4	83.3	100
GBL 11-20-14	-12.3	5.5	400	3.8	84.8	2.3	64.5	2.7	72.8	100
GBL 11-27-14	-26.8	8.0	400	9.0	86.0	5.8	58.0	7.0	76.3	100
GBL 06-06-15	14.9	9+	379	9.9	99.7	9.9	100.0	9.9	99.2	100
GBL 06-11-15	14.5	9+	400	9.8	98.5	9.8	98.8	9.8	98.8	91
GBL 06-18-15	11.2	9.0	400	9.0	99.5	9.0	97.8	8.9	98.5	76
GBL 07-01-15	14.8	5.5	400	1.2	87.5	0.3	94.0	0.7	91.3	100
GBL 10-29-15	-2.6	1.0	400	0.1	96.5	0.0	98.8	0.0	98.5	100
GBL 11-05-15	-12.1	2.0	400	0.8	96.0	0.5	88.5	0.3	92.3	95
GBL 11-12-15	-14.9	2.0	400	1.5	88.3	0.6	83.3	1.0	85.5	100
GBL 11-19-15	-25.4	3.0	400	2.7	88.3	1.7	83.8	0.9	75.8	96
GBL 11-26-15	-8.4	6.5	400	5.6	77.3	3.3	67.5	3.9	69.5	91
GBL 12-02-15	-14.6	8.0	400	8.5	96.8	5.3	70.8	6.9	77.0	100
GBL 06-10-16	14.1	9.0	400	9.2	97.5	9.1	98.5	9.0	98.5	100
GBL 06-17-16	7.4	6.0	400	6.7	95.0	6.3	95.0	5.9	88.5	100
GBL 06-29-16	18.2	0.5	400	0.6	96.3	0.6	95.3	0.5	95.5	91
GBL 06-30-16	18.3	0.5	400	0.5	93.3	0.1	97.3	0.1	97.0	75

Table 6.1.3 Results of IRGS, *k*-means, and GMM classifications on GSL. Total ice cover fraction as well as overall classification accuracy (OA) are presented. Temperature, FDD/TDD, and percent lake included in the scene are also recorded.

Image ID	Temp (°C)	CIS	# of Samples	IRGS	OA (%)	K-means	OA (%)	GMM	OA (%)	% Lake Included
GSL 10-30-13	2.1	0.5	400	0.2	95.5	0.0	96.8	0.0	96.8	84
GSL 11-06-13	-4.7	0.5	400	0.5	93.0	0.1	92.5	0.1	93.0	97
GSL 11-07-13	-6.6	0.5	400	0.9	95.0	0.1	90.8	0.5	91.5	78
GSL 11-20-13	-22.9	3.0	400	3.0	76.3	1.4	65.3	2.1	67.8	78
GSL 12-05-13	-27.9	9.0	400	7.0	67.3	5.7	56.8	6.5	65.3	100
GSL 05-29-14	11.1	9.0	400	9.6	98.0	9.9	98.8	9.8	98.8	100
GSL 06-05-14	5.4	8.5	400	8.3	96.8	7.3	80.5	8.4	94.5	91
GSL 06-06-14	6.8	8.5	400	8.0	95.0	7.5	90.5	8.1	96.0	79
GSL 06-12-14	8.9	4.5	400	5.4	87.8	6.0	82.3	5.7	88.0	79
GSL 06-13-14	13.4	4.5	400	3.7	90.8	3.4	91.5	3.6	92.0	92
GSL 10-23-14	1.6	0.5	400	0.2	94.5	0.0	97.5	0.0	96.8	92
GSL 11-06-14	-3.4	0.5	400	0.4	93.0	0.0	92.3	0.3	92.8	100
GSL 11-20-14	-10.8	2.5	400	2.8	86.0	2.3	70.8	3.5	73.8	95
GSL 11-21-14	-16.8	2.5	400	4.3	96.0	2.3	81.0	3.4	82.3	75
GSL 11-28-14	-27.4	6.0	400	7.4	93.5	4.6	68.3	4.6	67.5	84
GSL 12-12-14	-18.5	9+	400	9.1	92.5	10.0	99.3	10.0	99.3	100
GSL 05-29-15	7.6	6.5	400	5.4	91.8	5.3	91.0	5.6	92.8	93
GSL 06-06-15	18.2	1.0	400	0.2	98.0	0.2	96.0	0.2	97.5	78
GSL 10-28-15	-2.8	1.0	400	0.3	97.5	0.3	97.8	0.4	98.0	74
GSL 10-29-15	-1.2	1.0	400	0.5	91.8	3.0	70.3	3.0	72.3	78
GSL 11-13-15	-5.1	2.0	400	1.0	94.0	0.3	90.5	0.4	91.0	83
GSL 11-27-15	-7.7	4.5	400	4.0	75.3	3.5	66.0	2.6	66.3	75
GSL 12-02-15	-9.8	4.5	400	4.4	85.8	3.9	69.5	4.2	67.8	100
GSL 12-04-15	-10.3	4.5	400	3.7	84.5	1.8	72.3	2.4	74.3	82
GSL 12-10-15	-10.9	5.0	400	6.1	92.5	3.7	75.5	4.9	83.8	75
GSL 12-17-15	-20.8	8.5	400	7.5	84.8	7.3	78.8	4.3	59.3	95
GSL 05-13-16	6.6	9+	400	9.5	98.0	9.6	99.0	9.8	99.0	79
GSL 05-18-16	2.9	7.0	400	8.5	95.8	7.5	84.0	8.0	91.3	86
GSL 05-19-16	2.0	7.0	400	7.5	98.0	7.4	96.8	7.5	98.8	75
GSL 05-26-16	7.6	5.5	400	4.3	95.3	3.6	92.5	4.2	94.5	82
GSL 06-02-16	12.0	2.5	400	1.5	95.0	1.4	94.0	1.3	94.5	79

6.2 Comparison with CIS Weekly Ice Cover Fractions

Figures 6.2.1 and 6.2.2 display total ice fractions from IRGS, *k*-means, and GMM classification methods as well as those provided by CIS for GBL and GSL over the three years studied. The IRGS approach most closely follows the CIS fraction line, however the all of tested methods often display a lower ice cover fraction than recorded by CIS. This difference is likely do to the overestimation of open water (ice error) by all methods tested, as well as the tendency for CIS analysts to overestimate the amount of ice in a lake. (V. Pinard, personal communication, 2017). Overall, the tested methods closely follow the reported fractions from CIS, with phenology events following a similar trend as that recorded by ice analysts.

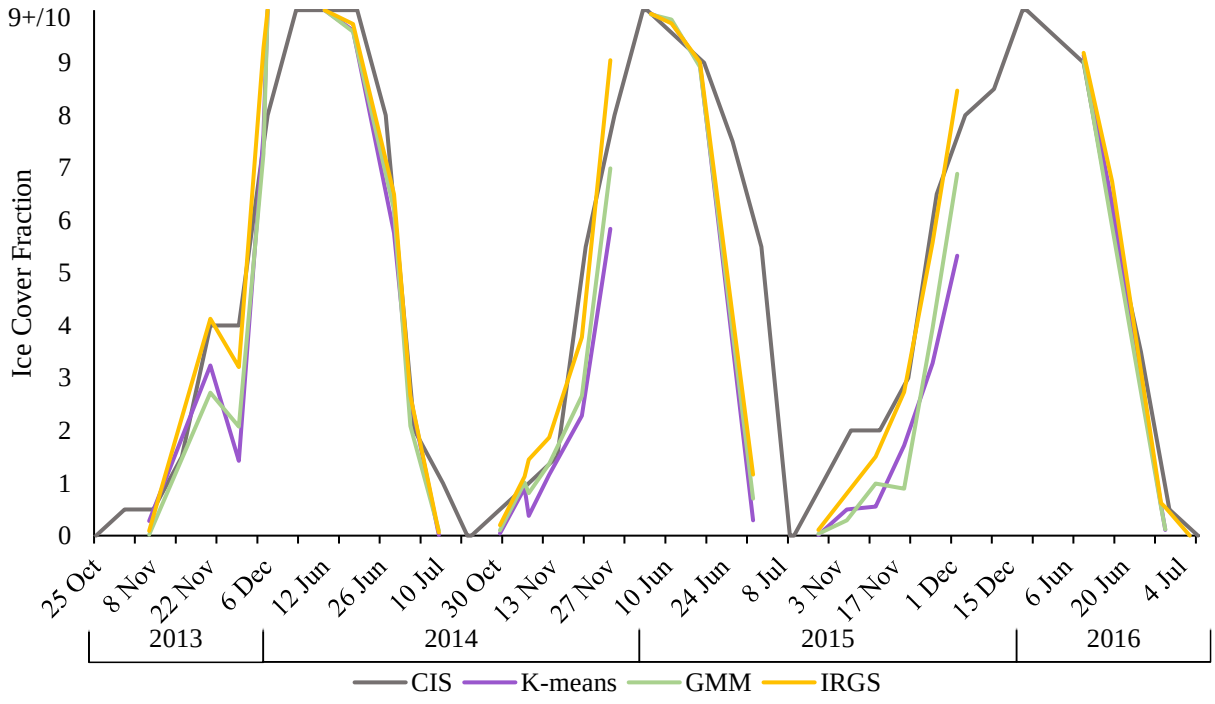

Figure 6.2.1 Total ice cover fractions for GBL from each classification method compared with estimates provided by CIS. Winter and summer months where the lake is completely ice covered or completely ice free are omitted.

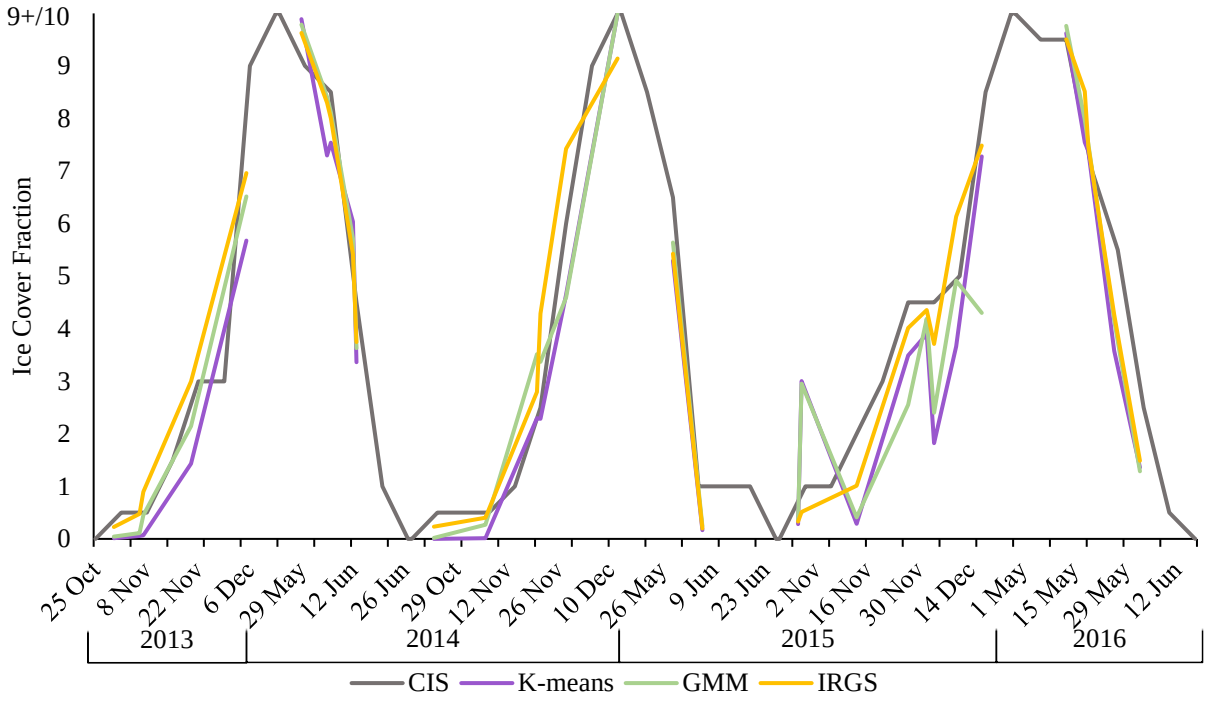

Figure 6.2.2 Total ice cover fractions for GSL from each classification method compared with estimates provided by CIS. Winter and summer months where the lake is completely ice covered or completely ice free are omitted.

Discrepancies between the methods tested and the reported CIS fractions largely occur during freeze-up which is congruent with lower classification accuracies observed during that time. The most prominent examples of this are shown in Figure 6.2.2 during the fall of 2015. Two notable deviations from the CIS ice fraction are recorded during that time. First, the *k*-means and GMM segmentations show a spike in total ice cover early in the fall which does not match reports from CIS. The two methods record total ice cover jumping to ~30% in late October and then receding back to less than 10% before refreezing. This is caused by an over estimation of ice due to incidence angle variation in the HH polarized SAR scene of October 29th. This is shown in Figure 6.2.3 where low backscatter of open water in the east arm of the lake has caused it to be separated from open water in the central basin for these two methods.

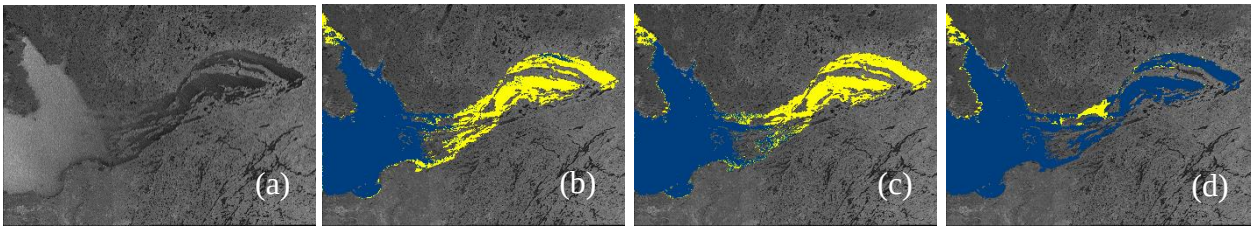

Figure 6.2.3 Effect of incidence angle on *k*-means and GMM segmentation approaches in GSL scene from October 29th, 2015. (a) HH polarized SAR image (b) K-means segmentation, (c) GMM segmentation, (d) Glocal IRGS segmentation.

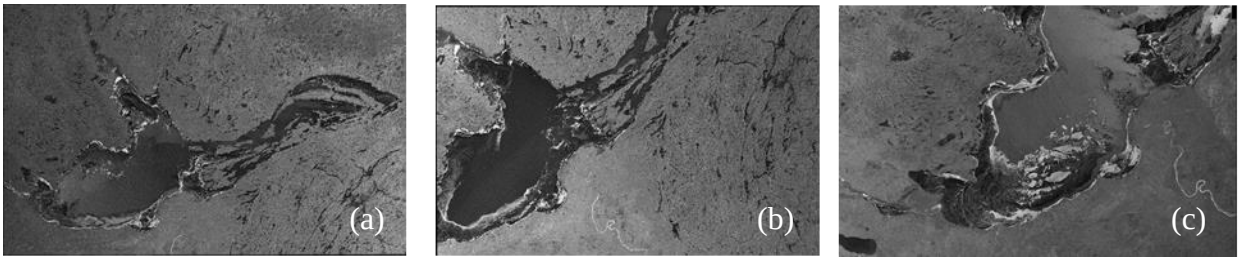

Figure 6.2.4 Evolution of freeze-up on GSL, 2015 (a) HH image from December 2nd, (b) HH image from December 4th, (c) HH image from December 10th.

The second deviation comes later in the season, where all three of the tested methods show a decrease in ice cover in early December. The three scenes in question are displayed in Figure 6.2.4. It is likely that this decrease in ice cover is correctly reflected by the tested methods as regions of ice may have been pushed into the northern shore of the lake by wind between December 2nd and December 4th, causing the drop in ice cover fraction. This may also be a product of the fact that less of the lake is included in the scene where ice is present (82% on December 4th compared to 100% on December 2nd).

Figures 6.2.5 and 6.2.6 display the difference between the total ice fraction resulting from the IRGS approach and the CIS recorded ice fraction. These figures show that the ice cover fraction from IRGS is very similar to that reported from CIS, differing less than 2/10ths in most cases and having an average difference of -0.2/10 for all scenes. A larger variation is recorded for the scene of GBL on July 1st, 2015 where IRGS reported total ice coverage of 1.2 while the recorded fraction

from CIS was 5.5/10. This scene is displayed in Figure 6.2.7 along with the IRGS result which fairly accurately captures the amount of ice present. The higher estimation of ice by CIS may be a result of analysts' tendency to over-estimate ice, an error, or some other unknown reason.

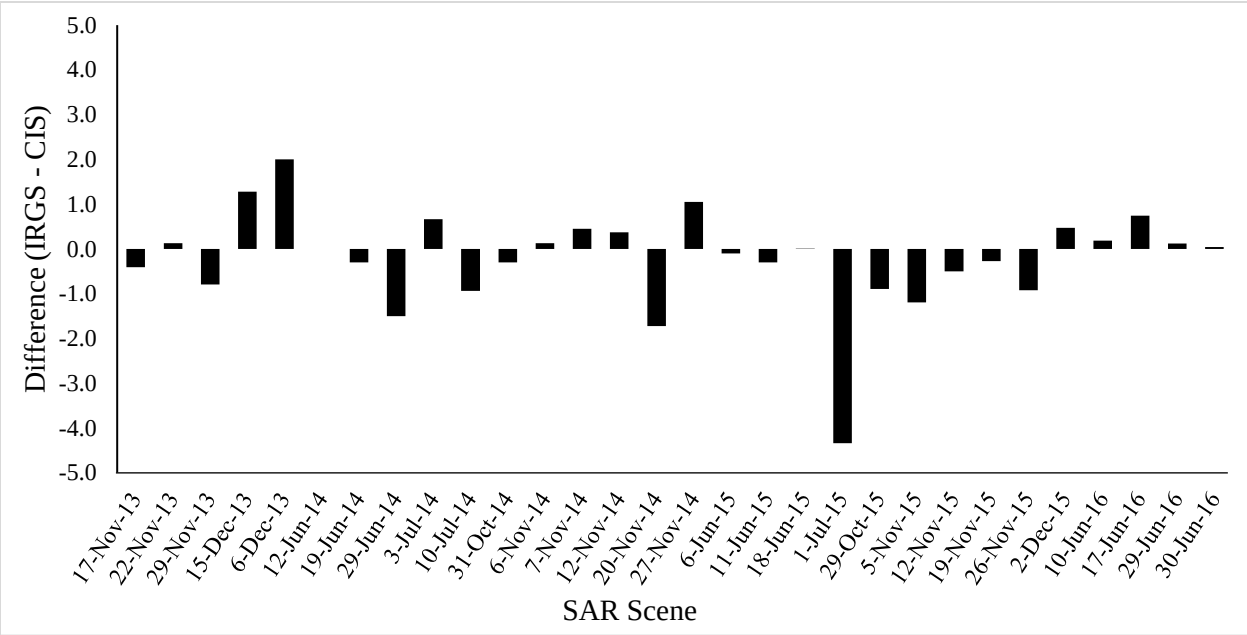

Figure 6.2.5 Difference in ice fraction (IRGS-CIS) for each tested scene of GBL.

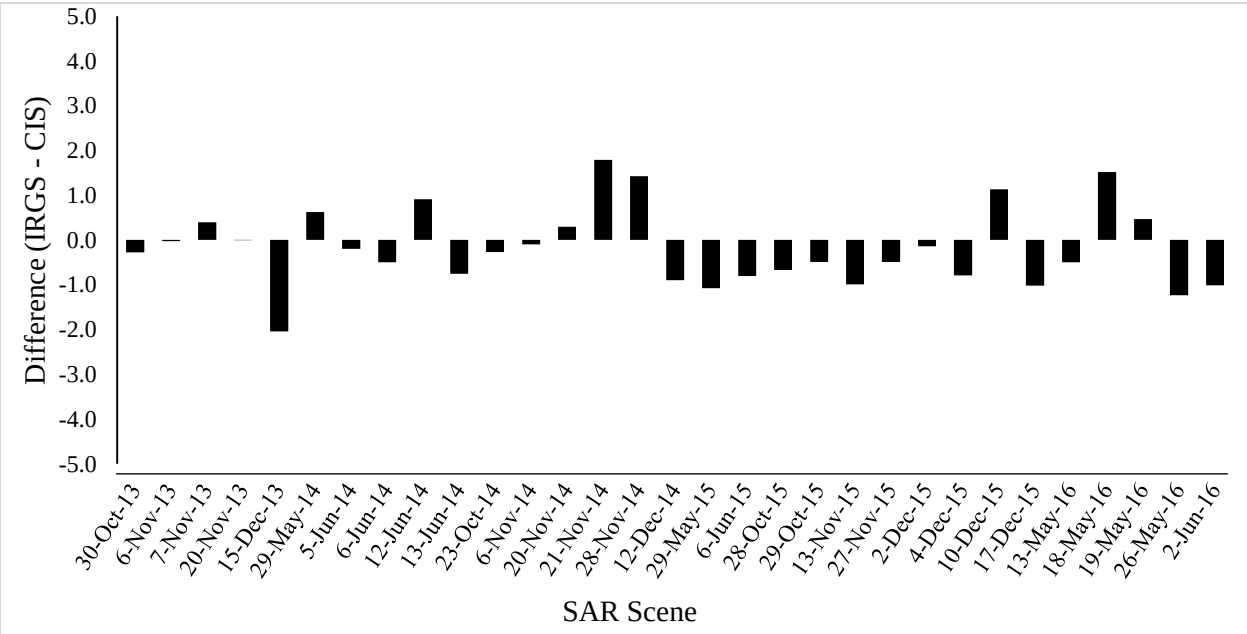

Figure 6.2.6 Difference in ice fraction (IRGS-CIS) for each tested scene of GSL.

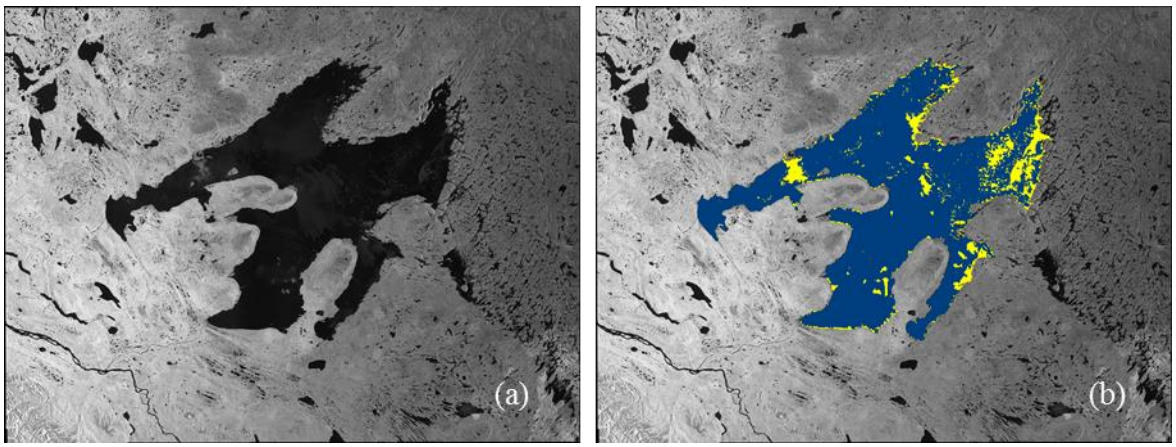

Figure 6.2.7 Scenes of GBL on July 1st, 2015, (a) HH polarized scene (b) IRGS classification approach result. Accuracy of IRGS result is 86.2%.

The complete freeze-up and break-up evolution for GSL during the winter of 2015-2016 as classified by the Glocal IRGS approach is presented in Figure 6.2.5. This particular season makes for an interesting visualization because it has the highest number of scenes available for a single year within the dataset, creating a detailed ice phenology record for the lake. This captures the potential of more detailed records of lake ice phenology which could be recorded, as it showcases the evolution and location of ice growth and decay on the lake in addition to providing total ice fraction. From this figure one can see that ice growth begins in the northern-most arm of the lake and continues along the shoreline with the central basin and deep east arm freezing last. In spring, break up begins at the Slave River inflow and Mackenzie River outflow. A similar pattern can be observed in Appendix 1.4 and 1.5 where the evolution of ice cover on GSL for the 2013-2014 and 2014-2015 seasons are included. This level of detail cannot be not captured operationally without the use of an automated classification method, especially considering the increased availability of SAR scenes from newly launched or planned observation missions. Similar products for the other ice cover seasons on GBL included in Appendix 1.1 – 1.3 and give interesting insight on the phenology of ice cover on these lakes.

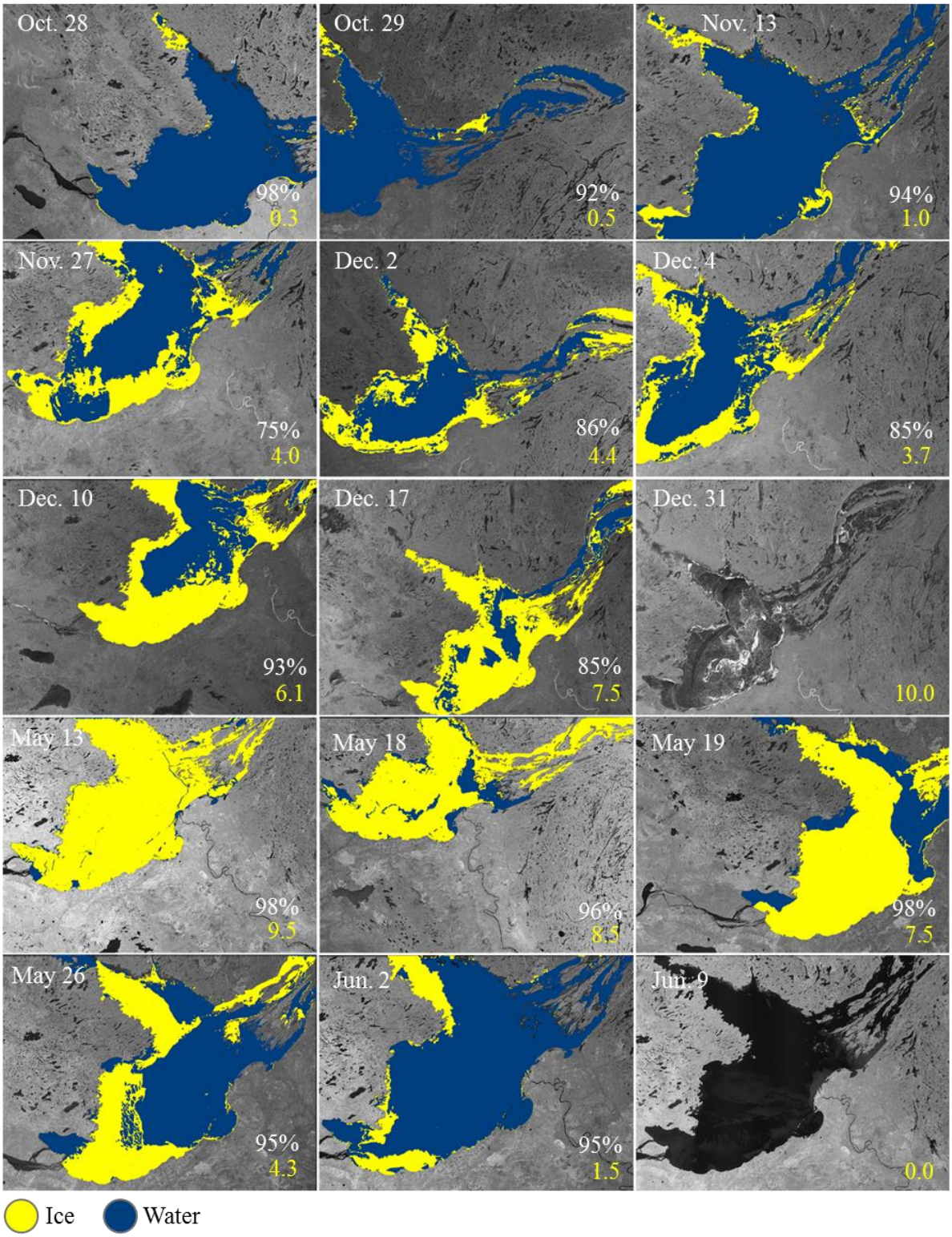

Figure 6.2.8 Evolution of freeze-up and break-up on GSL during the winter of 2015-2016 from IRGS results. Overall accuracy (white) and total ice cover fraction (yellow) is displayed the bottom right corner of each window. Scenes on December 31st and July 9th are included to show the timing of complete freeze-up and complete melt. The average overall accuracy of this image set is 91.4%.

7.0 Conclusion

Automated ice-water classification using SAR imagery is a difficult but necessary task for monitoring lake ice. In this work 61 RADARSAT-2 images of GBL and GSL are classified using *k*-means and GMM standard classification methods as well as the Glocal IRGS approach. Results confirm that variations in incidence angle within a scene cause errors in ice-water classification using standard methods, and that ice types with low backscatter signatures such as thin new ice are not well classified by these methods.

The Glocal IRGS segmentation method including initial autopolygon creation, accounts for the challenges presented when segmenting ice and water, and various studies have validated the ability of this method to produce highly accurate and reliable results (Yu & Clausi, 2007; 2008; Leigh et al., 2014). In this study the semi-automated IRGS approach performed very well during both freeze-up and break-up, resulting in an overall accuracy of 92.1%. Glocal IRGS shows promise as a means of quickly and accurately processing SAR data for lake ice monitoring in the future, however automated labeling through the use of SVM or other means will need be incorporated with this method for it to be suitable operationally. This added functionality will minimize user input, an essential advance for processing the vast amount of imagery becoming available from recently launched and upcoming SAR missions including Sentinel 1 A/B and the RADARSAT Constellation.

The literature describes that climate change and air temperature variability can be reliably indicated by lake ice phenology and has been the focus of several studies (Duguay et al. 2003; Magnuson, 2000). Other works have related social, economic, and environmental spheres to lake ice cover, making clear the importance of studying lake ice phenology (Prowse et al., 2011b). Recorded and projected climate change will have a strong impact on the factors that influence lake

ice phenology, causing an overall change to the cycle of ice formation and decay. These factors further add to the importance of developing methods to reliably monitor lake ice in the coming years.

8.0 Recommendations for Future Work

Recently, ice-water class labels have been successfully generated along with segmentation in studies of sea ice by using texture information in addition to backscatter values from the HH and HV polarizations. These methods then employ a support vector machine (SVM) classifier to produce a label for each segmented area based on GLCM texture information. A procedure for generating this information is available in MAGIC for use with IRGS. This process involves manually labeling a given number of pixels in each SAR image of a selected set, then running a forward-feature search to determine the texture features from a candidate set which will provide the minimum average error in an SVM classification. This set can then be used in SVM classification to assign ice-water labels to previously segmented regions (Leigh et al., 2014).

This SVM approach is presented by Leigh et al. (2014) and was reported to be up to 97% accurate when tested on 20 scenes of sea ice, but has yet to be tested on scenes of lake ice. An SVM model using GLCM texture features was also employed by Zakhvatkina et al. (2017) in their study of 24 sea ice scenes near Greenland, where they reported up to 95% accuracy. For lake ice monitoring purposes, an automated or semi-automated classification technique such as one employing an SVM incorporating texture and backscatter information would allow for detailed records to be produced at a high volume. The accuracy and timeliness of such a technique would also need to be considered. A continuation of this work would incorporate labeling for the 61 scenes segmented with IRGS, as labeling pixels for GLCM selection was already completed to create the reference data for this study.

The coming RADARSAT Constellation mission (RCM) scheduled for launch this year will include sensors outfitted for the use of compact polarimetry data in wide swath modes. Dabboor

& Geldsetzer (2014) simulated 23 compact polarimetry parameters and tested them with a Maximum Likelihood classification in order to select the optimum parameter for sea ice type, and ice-water classification. In this study the authors were able to select a subset of parameters which produced very high accuracy classification for varying ice types (99.9%) and discrimination of ice and open water (100%). This study demonstrates the promising potential for the development automated ice-water classification additional information available in compact-polarimetric imagery. Embracing and studying this advancement data availability will be essential to further the monitoring lake ice phenology in the coming years.

References

Adams, W., & Roulet, N. (1980). Illustration of the roles of snow in the evolution of the winter cover of a lake. *Arctic*, 100-116.

Ashton, G. D. (2011). River and lake ice thickening, thinning, and snow ice formation. *Cold Regions Science and Technology, 68(1*-2), 3-19.

Bengtsson, L. (1986). Spatial variability of lake ice covers. *Geografiska Annaler Series A Physical Geography*, 113-121.

Bengtsson, L. (2012). Ice Formation on Lakes and Ice Growth. In *Encyclopedia of Lakes and Reservoirs* (pp. 360-361). Springer Netherlands.

Bonsal, B. R., Prowse, T. D., Duguay, C. R., & Lacroix, M. P. (2006). Impacts of large- scale teleconnections on freshwater-ice break/freeze-up dates over Canada. *Journal of Hydrology*, 330(1), 340-353.

Brown, L. C., & Duguay, C. R. (2010). The response and role of ice cover in lake-climate interactions. *Progress in Physical Geography*, 34(5), 671-704.

Brown, L. C., & Duguay, C. R. (2011). The fate of lake ice in the North American arctic. *The Cryosphere*, 5(4), 869.

Brown, R. D., Duguay, C. R., Goodison, B. E., Prowse, T. D., Ramsay, B., & Walker, A. E. (2002, December). Freshwater ice monitoring in Canada-an assessment of Canadian contributions for global climate monitoring. In Proc. 16th IAHR International Symposium on Ice, Dunedin, New Zealand (Vol. 1, pp. 368-376).

Castleman, K. R. (1996). *Digital image processing*. Englewood Cliffs, NJ: Prentice Hall.

Clausi, D. A., Qin, A. K., Chowdhury, M. S., Yu, P., & Maillard, P. (2010). MAGIC: MAp-guided ice classification system. *Canadian Journal of Remote Sensing*, 36, S13-S25.

Curry, J., Schramm, J., & Ebert, E. (1993). Impact of clouds on the surface radiation balance of the Arctic Ocean. *Meteorology and Atmospheric Physics*, 51(3), 197-217.

Dabboor, M., & Geldsetzer, T. (2014). Towards sea ice classification using simulated RADARSAT constellation mission compact polarimetric SAR imagery. *Remote Sensing of Environment*, 140, 189-195.

Duguay, C. R., Pultz, T. J., Lafleur, P. M., & Drai, D. (2002). RADARSAT backscatter characteristics of ice growing on shallow sub-Arctic lakes, churchill, manitoba, canada. *Hydrological Processes*, 16(8), 1631-1644.

Duguay, C. R., Flato, G. M., Jeffries, M. O., Ménard, P., Morris, K., & Rouse, W. R. (2003). Ice-cover variability on shallow lakes at high latitudes: Model simulations and observations. *Hydrological Processes*, 17(17), 3465-3483.

Duguay, C. R., Prowse, T. D., Bonsal, B. R., Brown, R. D., Lacroix, M. P., & Ménard, P. (2006). Recent trends in canadian lake ice cover. *Hydrological Processes*, 20(4), 781-801.

Gauthier, Y., Tremblay, M., Bernier, M., & Furgal, C. (2010). Adaptation of a radar-based river ice mapping technology to the Nunavik context. *Canadian Journal of Remote Sensing*, 36(sup1), S168-S185.

Geldsetzer, T., & van der Sanden, J. (2013). Identification of polarimetric and nonpolarimetric C-band SAR parameters for application in the monitoring of lake ice freeze-up. *Canadian Journal of Remote Sensing*, 39(3), 263-275.

Gill, R. S. (2003, April). SAR ice classification using fuzzy screening method. In *Applications of SAR Polarimetry and Polarimetric Interferometry* (Vol. 529).

Ghanbari, R. N., Bravo, H. R., Magnuson, J. J., Hyzer, W. G., & Benson, B. J. (2009). Coherence between lake ice cover, local climate and teleconnections (Lake Mendota, Wisconsin). *Journal of Hydrology*, 374(3), 282-293.

Haverkamp, D., Soh, L. K., & Tsatsoulis, C. (1993). A dynamic local thresholding technique for sea ice classification. *Geoscience and Remote Sensing Symposium, 1993. IGARSS'93. Better Understanding of Earth Environment., International*, pp. 638-640.

Heron, R., & Woo, M. (1994). Decay of a high arctic lake-ice cover: Observations and modelling. *Journal of Glaciology*, 40(135), 283-292.

Holmes, Q. A., Nuesch, D. R., & Shuchman, R. A. (1984). Textural analysis and real-time classification of sea-ice types using digital SAR data. *IEEE Transactions on Geoscience and Remote Sensing*, (2), 113-120.

Howell, S. E., Brown, L. C., Kang, K., & Duguay, C. R. (2009). Variability in ice phenology on Great Bear Lake and great slave lake, northwest territories, Canada, from SeaWinds/QuikSCAT: 2000–2006. *Remote Sensing of Environment*, 113(4), 816-834.

Jain, A. K., Murty, M. N., & Flynn, P. J. (1999). Data clustering: A review. *ACM Computing Surveys (CSUR)*, 31(3), 264-323.

Jain, A. K. (2010). Data clustering: 50 years beyond K-means. *Pattern Recognition Letters*, 31(8), 651-666.

Jeffries, M. O., Morris, K., & Duguay, C. R. (2012). Floating ice: Lake ice and river ice. *Satellite Image Atlas of Glaciers of the World.Vol.A: State of the Earth's Cryosphere at the Beginning of the 21st Century: Glaciers, Global Snow Cover, Floating Ice, and Permafrost and Periglacial Environments:* U.S. Geological Survey Professional Paper 1386-A, pp. A381-A424.

Jeffries, M. O., Morris, K., & Kozlenko, N. (2005). Ice characteristics and processes, and remote sensing of frozen rivers and lakes. *Remote sensing in northern hydrology: Measuring environmental change* (pp. 63-90) American Geophysical Union.

Jones, J. A. A. (1969). The growth and significance of white ice at knob lake, Quebec. *The Canadian Geographer/Le Géographe Canadien*, 13(4), 354-372.

Karvonen, J., Simila, M., & Makynen, M. (2005). Open water detection from Baltic Sea ice Radarsat-1 SAR imagery. *IEEE Geoscience and Remote Sensing Letters*, 2(3), 275-279.

Kellndorfer, J. M., & McDonald, K. C. (2009). Active and passive microwave systems. *The SAGE Handbook of Remote Sensing*, 179.

Kwok, R., Cunningham, G., & Holt, B. (1992). An approach to identification of sea ice types from spaceborne SAR data. *Microwave Remote Sensing of Sea Ice*, 68, 355-360.

Leigh, S., Wang, Z., & Clausi, D. A. (2014). Automated ice-water classification using dual polarization SAR satellite imagery. *IEEE Transactions on Geoscience and Remote Sensing*, 52(9), 5529-5539.

Lenormand, F., Duguay, C. R., & Gauthier, R. (2002). Development of a historical ice database for the study of climate change in Canada. *Hydrological Processes*, 16(18), 3707-3722.

Leshkevich, G., & Nghiem, S. V. (2013). Great lakes ice classification using satellite C-band SAR multi-polarization data. *Journal of Great Lakes Research*, 39, 55-64.

Li, F., Clausi, D. A., Wang, L., & Xu, L. (2015). A semi-supervised approach for ice-water classification using dual-polarization SAR satellite imagery. In *Proceedings of the IEEE Conference on Computer Vision and Pattern Recognition Workshops* (pp. 28-35).

Liu, H., Guo, H., & Zhang, L. (2015). SVM-based sea ice classification using textural features and concentration from RADARSAT-2 Dual-Pol ScanSAR data. *IEEE Journal of Selected Topics in Applied Earth Observations and Remote Sensing*, 8(4), 1601-1613.

Livingstone, D. M. (1997). Break-up dates of alpine lakes as proxy data for local and regional mean surface air temperatures. *Climatic Change*, 37(2), 407-439.

Livingstone, D. M., Adrian, R., Blenckner, T., George, G., & Weyhenmeyer, G. A. (2010). Lake ice phenology. In D. G. George (Ed.), *the impact of climate change on European lakes* (pp. 51-61) Springer.

MacDonald, Dettwiler and Associates Ltd. (2014). *RADARSAT-2 product description*. Richmond, B.C.:

Magnuson, J. J. (2000). Historical trends in lake and river ice cover in the northern hemisphere. *Science,* 291(5502), 254-254.

Morris, K., Jeffries, M., & Weeks, W. (1995). Ice processes and growth history on arctic and sub-arctic lakes using ERS-1 SAR data. *Polar Record,* 31(177), 115-128.

Nghiem, S. V., & Leshkevich, G. A. (2007). Satellite SAR remote sensing of great lakes ice cover, part 1. Ice backscatter signatures at C band. *Journal of Great Lakes Research,* 33(4), 722-735.

Palecki, M., & Barry, R. (1986). Freeze-up and break-up of lakes as an index of temperature changes during the transition seasons: A case study for finland. *Journal of Climate and Applied Meteorology,* 25(7), 893-902.

Pons Bernad, G., Denise, L., & Refregier, P. (2009). Hierarchical feature- based classification approach for fast and user-interactive SAR image interpretation. *Geoscience and Remote Sensing Letters, IEEE,* 6(1), 117-121.

Prowse, T., Alfredsen, K., Beltaos, S., Bonsal, B., Bowden, W., Duguay, C. R., et al. (2011a). Effects of changes in arctic lake and river ice. *Ambio,* 40(1), 63-74.

Prowse, T., Alfredsen, K., Beltaos, S., Bonsal, B., Duguay, C. R., Korhola, A., et al. (2011b). Arctic freshwater ice and its climatic role. *Ambio; Ambio,* 40, 46-52.

Ragotzkie, R. A. (1978). Heat budgets of lakes. In A. Lerman (Ed.), *Lakes - chemistry, geology, physics* (pp. 1-19). New York: Springer.

Ray, A., Kartikeyan, B., Garg, S., & HOD, C. Towards Identifying Optimal Quality Indicators for Evaluating De-Noising Algorithm Performance in SAR.

Robertson, D. M., Wynne, R. H., & Chang, W. (2000). Influence of El Niño on lake and river ice cover in the northern hemisphere from 1900 to 1995. *Verhandlugen Internationale Vereingung Fur Limnologie,* 27(5), 2784-2788.

Rouse, W. R., Blanken, P. D., Duguay, C. R., Oswald, C. J., & Schertzer, W. M. (2008). Climate-lake interactions. *Cold region atmospheric and hydrologic studies. The Mackenzie GEWEX experience* (pp. 139-160) Springer.

Schindler, D. W., Beaty, K. G., Fee, E. J., Cruikshank, D. R., Debruyn, E. R., Findlay, D. L., et al. (1990). Effects of climatic warming on lakes of the central boreal forest. *Science (New York, N.Y.),* 250(4983), 967-970.

Shokr, M., & Sinha, N. (2015). *Sea ice: Physics and remote sensing* (Geophysical monograph; 209). Washington, D.C.: Hoboken, New Jersey: American Geophysical Union; John Wiley & Sons.

Soh, L. K., & Tsatsoulis, C. (1999a). Texture analysis of SAR sea ice imagery using gray level co-occurrence matrices. *Geoscience and Remote Sensing, IEEE Transactions on,* 37(2), 780-795.

Soh, L. K., & Tsatsoulis, C. (1999b). Unsupervised segmentation of ERS and RADARSAT sea ice images using multiresolution peak detection and aggregated population equalization. *International Journal of Remote Sensing,* 20(15-16), 3087-3109.

Soh, L. K., Tsatsoulis, C., Gineris, D., & Bertoia, C. (2004). ARKTOS: An intelligent system for SAR sea ice image classification. *Geoscience and Remote Sensing, IEEE Transactions on,* 42(1), 229-248.

Sobiech, J., & Dierking, W. (2013). Observing lake-and river-ice decay with SAR: Advantages and limitations of the unsupervised k-means classification approach. *Annals of Glaciology,* 54(62), 65-72.

Surdu, C. M., Duguay, C. R., Pour, H. K., & Brown, L. C. (2015). Ice Freeze-up and Break-up Detection of Shallow Lakes in Northern Alaska with Spaceborne SAR. *Remote Sensing*, 7(5), 6133-6159.

Tso, B. (2001). In Mather P. M. (Ed.), *Classification methods for remotely sensed data*. London; New York: Taylor & Francis.

Vincent, L., & Soille, P. (1991). Watersheds in digital spaces: An efficient algorithm based on immersion simulations. *Pattern Analysis and Machine Intelligence, IEEE Transactions on*, 13(6), 583-598.

Wang, L., Scott, K. A., & Clausi, D. A. (2016). Improved sea ice concentration estimation through fusing classified SAR imagery and AMSR-E data. *Canadian Journal of Remote Sensing*, 42(1), 41-52.

Weber, F., Nixon, D., & Hurley, J. (2003). Semi-automated classification of river ice types on the Peace River using RADARSAT-1 synthetic aperture radar (SAR) imagery. *Canadian Journal of Civil Engineering*, 30(1), 11-27.

Williams, G. P. (1965). Correlating freeze-up and break-up with weather conditions. *Canadian Geotechnical Journal*, 2(4), 313-326.

Williams, G., Layman, K. L., & Stefan, H. G. (2004). Dependence of lake ice covers on climatic, geographic and bathymetric variables. *Cold Regions Science and Technology*, 40(3), 145-164.

Yu, Q., & Clausi, D. A. (2007). SAR sea-ice image analysis based on iterative region growing using semantics. *IEEE Transactions on Geoscience and Remote Sensing*, 45(12), 3919-3931.

Yu, Q., & Clausi, D. A. (2008). IRGS: Image segmentation using edge penalties and region growing. *IEEE transactions on pattern analysis and machine intelligence*, 30(12), 2126-2139.

Yu, P., Qin, A. K., & Clausi, D. A. (2012). Unsupervised polarimetric SAR image segmentation and classification using region growing with edge penalty. *IEEE Transactions on Geoscience and Remote Sensing*, 50(4), 1302-1317.

Zakhvatkina, N. Y., Alexandrov, V. Y., Johannessen, O. M., Sandven, S., & Frolov, I. Y. (2013). Classification of sea ice types in ENVISAT synthetic aperture radar images. *IEEE Transactions on Geoscience and Remote Sensing*, 51(5), 2587-2600.

Zakhvatkina, N., Korosov, A., Muckenhuber, S., Sandven, S., & Babiker, M. (2017). Operational algorithm for ice–water classification on dual-polarized RADARSAT-2 images. *The Cryosphere*, 11(1), 33.

Appendix 1

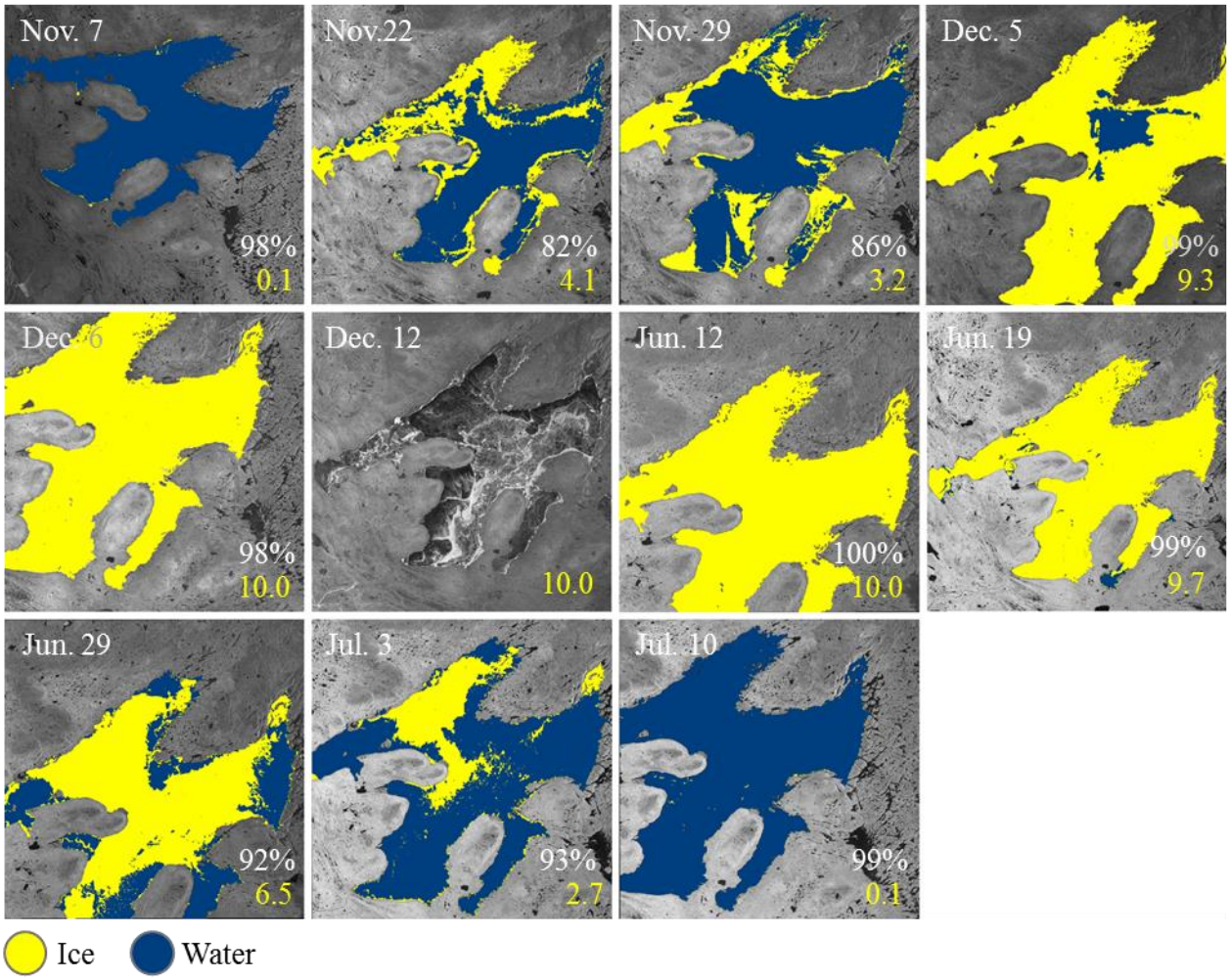

Appendix 1.1 Evolution if freeze-up and break-up on GBL during the winter of 2013-2014 from IRGS results. Overall accuracy (white) and total ice cover fraction (yellow) is displayed the bottom right corner of each window. Scene from December 12th is included to show the timing of complete freeze-up.

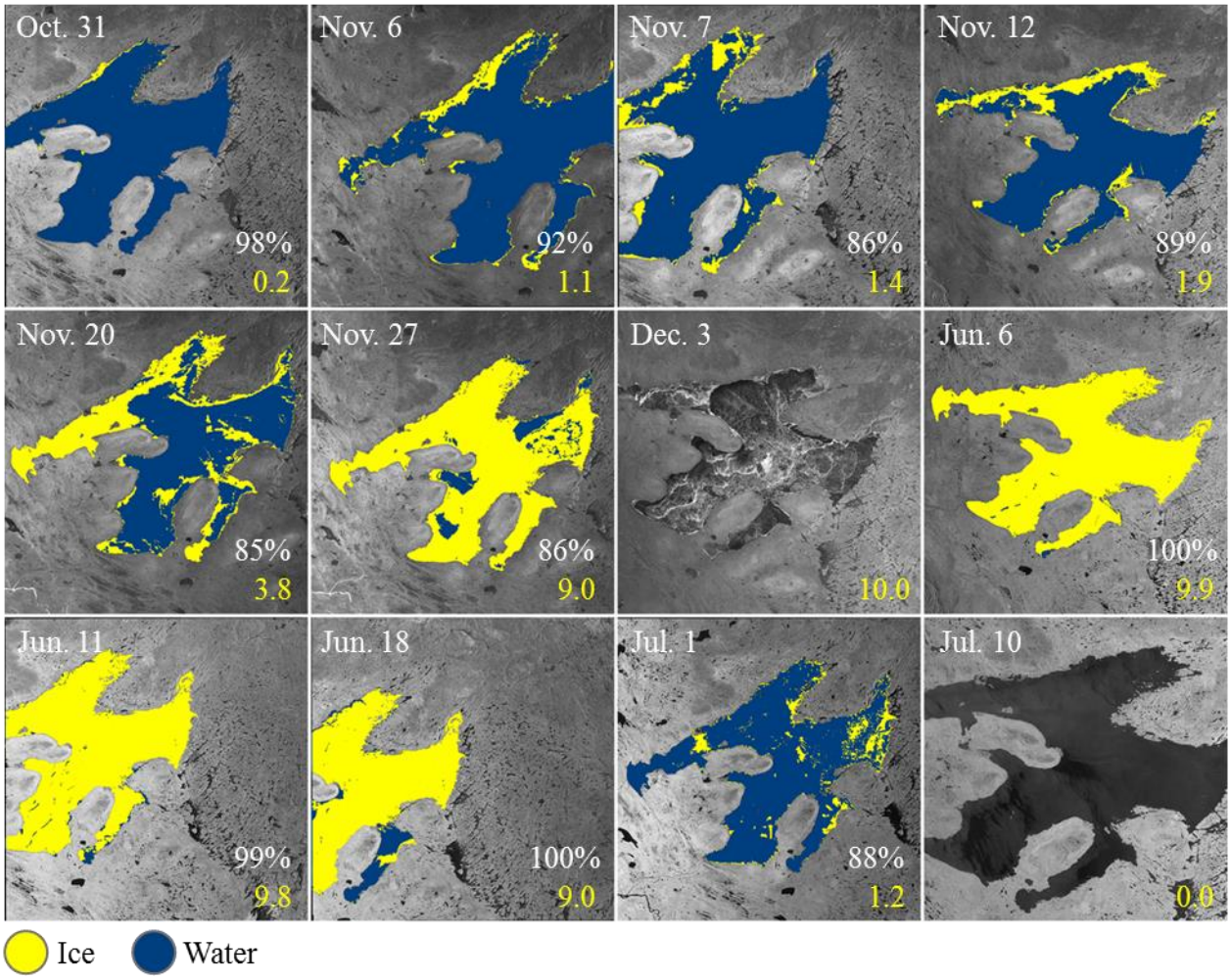

Appendix 1.2 Evolution if freeze-up and break-up on GBL during the winter of 2014-2015 from IRGS results. Overall accuracy (white) and total ice cover fraction (yellow) is displayed the bottom right corner of each window. Scenes on December 3rd and July 10th are included to show the timing of complete freeze-up and complete melt.

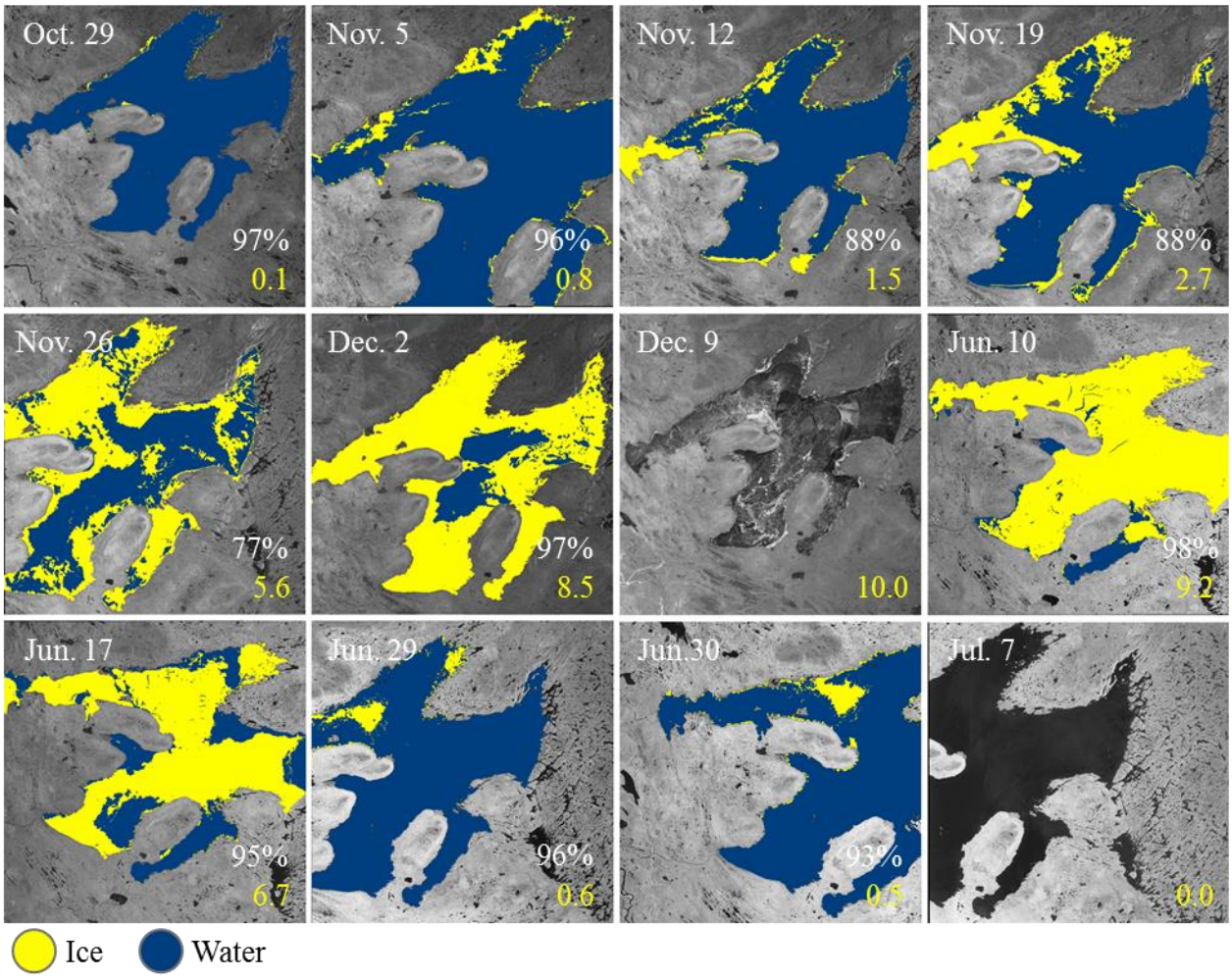

Appendix 1.3 Evolution if freeze-up and break-up on GBL during the winter of 2015-2016 from IRGS results. Overall accuracy (white) and total ice cover fraction (yellow) is displayed the bottom right corner of each window. Scenes on December 9th and July 7th are included to show the timing of complete freeze-up and complete melt.

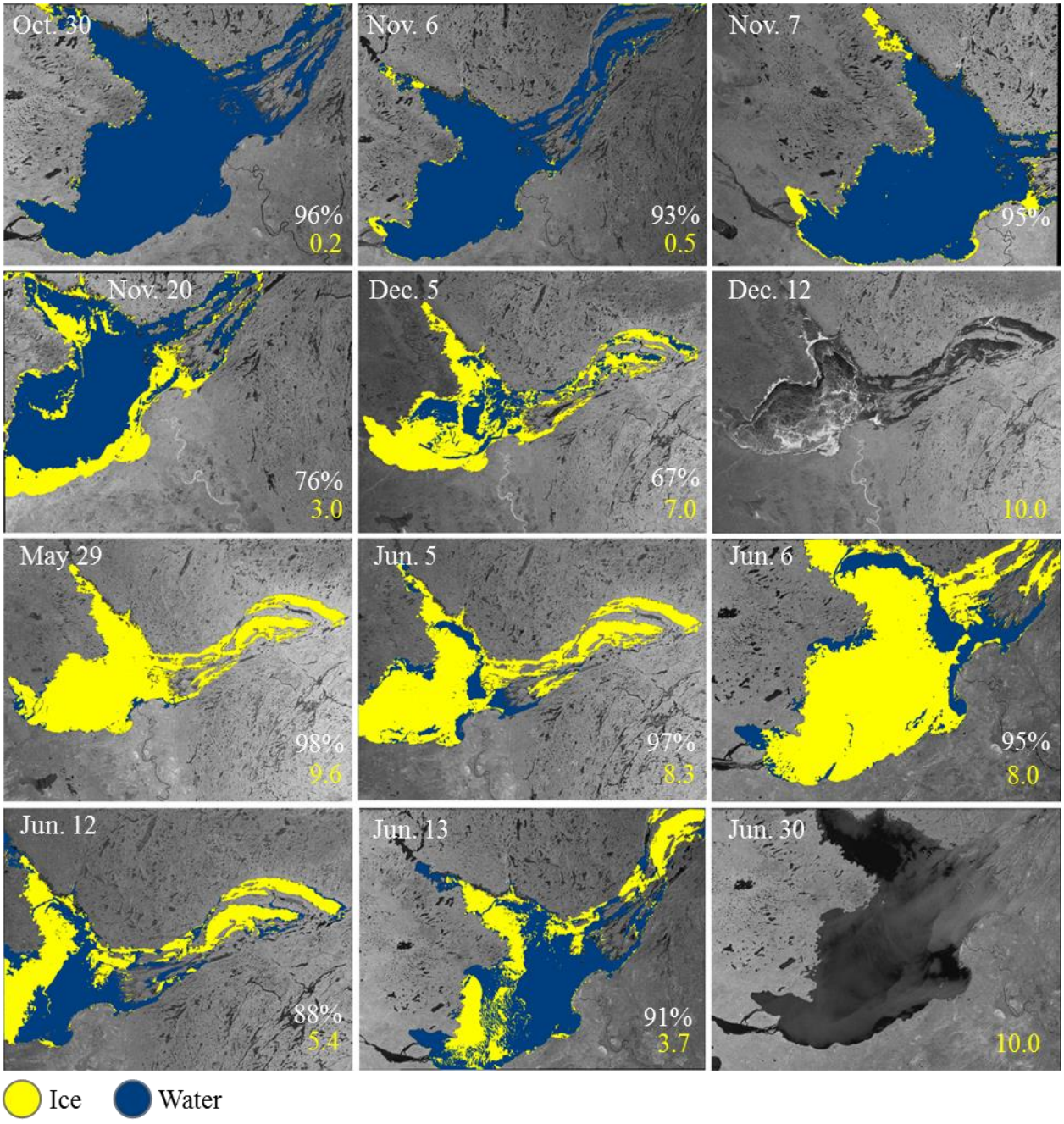

Appendix 1.4 Evolution if freeze-up and break-up on GSL during the winter of 2013-2014 from IRGS results. Overall accuracy (white) and total ice cover fraction (yellow) is displayed the bottom right corner of each window. Scenes on December 12th and June 30th are included to show the timing of complete freeze-up and complete melt.

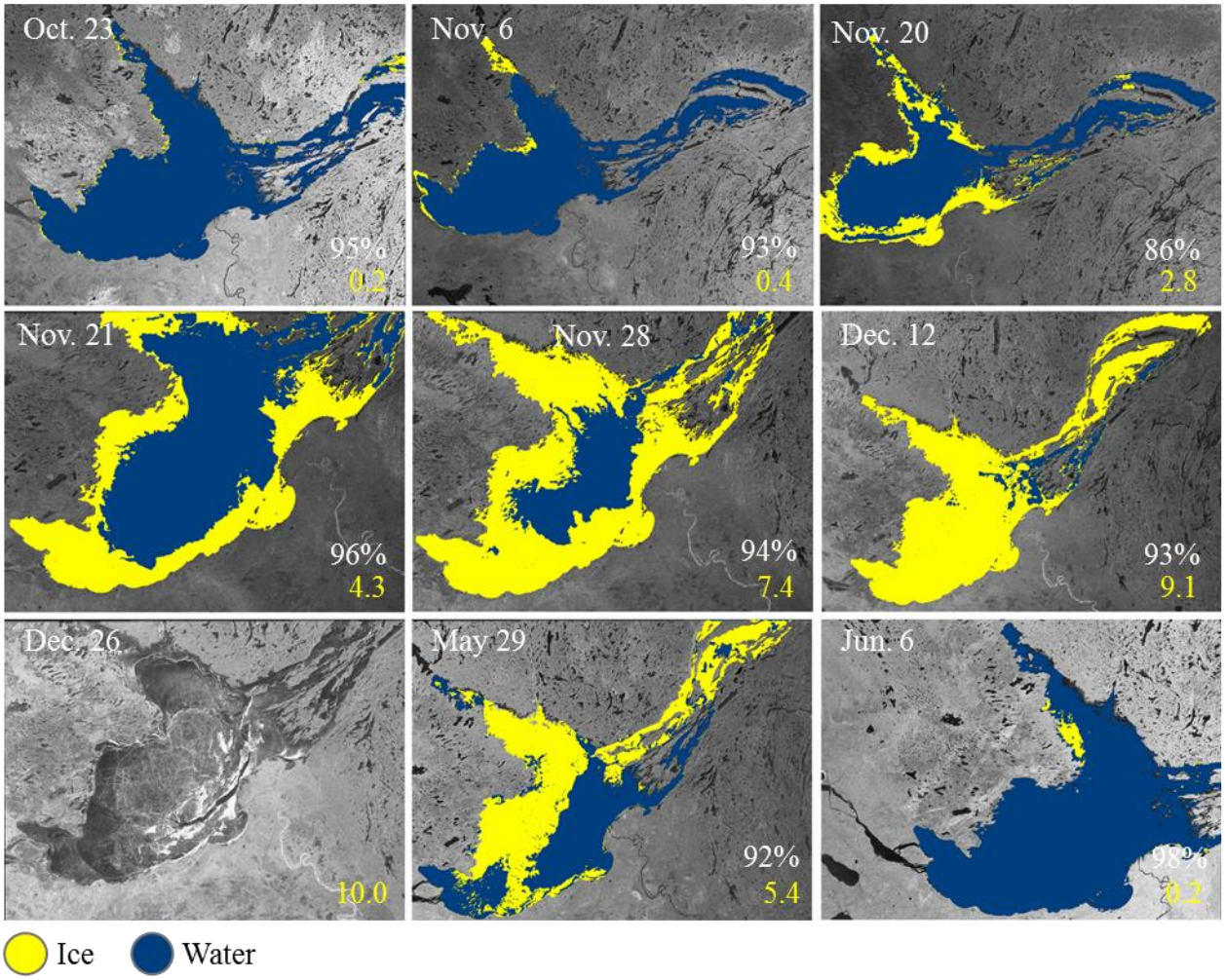

Appendix 1.5 Evolution if freeze-up and break-up on GSL during the winter of 2014-2015 from IRGS results. Overall accuracy (white) and total ice cover fraction (yellow) is displayed the bottom right corner of each window. Scenes on December 26th is included to show the timing of complete freeze-up.